Nanostructure Engineering for Photovoltaics

by

Qiuyang Xiong

A thesis submitted in partial fulfillment of the requirements for the degree of

Master of Science
in
Photonics and Plasmas

Department of Electrical and Computer Engineering Faculty of Engineering
University of Alberta

Abstract

The lead sulfide colloidal quantum dots (PbS CQD) solar cell has attracted wide attention in recent years for its facile fabrication process and low cost. However, the power conversion efficiency (PCE) of PbS CQD cell is still low due to the trade-off between light absorption and carrier collection inside the absorption layer. The advancement of light trapping techniques has provided a solution to improve the PCE by increasing light absorption capability. In this thesis, two-dimensional (2D) periodic nanostructures have been fabricated using nanosphere lithography (NSL) and the fabrication process is optimized for large area and high quality nanostructures. To achieve light trapping, the fabricated structures are designed as two kinds: the metallic structure and the dielectric structure. The metallic structure can be used as the back reflector in solar cells and the dielectric structure made with conductive materials can be used as the transparent electrode. The surface plasmon (SP) modes excited on metallic nanostructures have been investigated and their applications for solar cells are discussed. For the dielectric structure, PbS CQD solar cells incorporated with patterned indium-doped tin oxide (ITO) electrodes are numerically studied with finite-difference time-domain (FDTD) simulation. More than 10% overall absorption enhancement has been achieved with the presence of fabricated nanostructures.

Preface

The dissertation is submitted for the degree of the Master of Science at the University of Alberta. This Master thesis contains results of the research undertaken in the Department of Electrical and Computer Engineering, University of Alberta, from January 2014 to June 2016, under the supervision of Professor Xihua Wang.

The experiment design and conducting in the chapter 2 was mainly done by myself with the equipment in our lab and the nanoFAB under the guidance of Prof. Xihua Wang. Prof. Jue Wei carried out part of the experimental work and offered great ideas for the problems encountered during the experiments.

Chapter 3 of this thesis has been published as Q. Xiong, J. Wei, S. M. Mahpeykar, L. Meng and X. Wang. "*Observation of localized surface plasmons and hybridized surface plasmon polaritons on self-assembled two-dimensional nanocavities,*" Opt. Lett., vol. 41, issue 7, 1506-1509. I was the first author of the in this paper. J. Wei, S. M. Mahpeykar, L. Meng participated in the sample fabrication. X. Wang was the corresponding author.

Chapter 4 of this thesis has been published as J. Wei, Q. Xiong, S. M. Mahpeykar and X. Wang. "*Numerical study of complementary nanostructures for light trapping in colloidal quantum dot solar cells,*" Nanomaterial, vol. 6, issue 4. I was responsible for the simulation work and part of the sample fabrication. J. Wei and X. Wang designed the experiment, S. M. Mahpeykar was involved in the analysis of experimental results.

Acknowledgements

Even now I can hardly believe that my life as a Master student at the University of Alberta is about to come to the end. The night is deep, but I am not dreaming. The weekly reports left in the computer get everything recorded and remain me of every details in the two and a half years. I feel so grateful for everyone who accompanied me all the way through my Master degree, it is your presence making this span of my life colorful and memorable.

Foremost, I want to express my deep thanks to my supervisor Professor Xihua Wang, whom I also regard as my most respectful teacher and wise friend. His unreserved guidance and patience has led me through barriers and the struggles during my research. His continuous encouragement and guidance always help me to move forward. His profound instruction for both academic and life will definitely help me a lot in my future career. I would like to deliver my sincerest appreciation to Professor Jue Wei. It is my great honor to get the chance to work with the respectable pioneering scholar on my academic road. I have learned a lot from his rigorous altitude and integrity towards every step in the experiment. My appreciations also go to the rest of my committee, Professor Sandipan Pramanik and Professor Ray DeCorby.

All the results described in this thesis was accomplished with the support and help of my labmates. I was greatly benefited from their keen scientific insight in every group discussion. The ideas can always inspire new thoughts in my mind and help me solve the problems. My deepest thanks go to my colleagues: Seyed Milad Mahpeykar, Lingju Meng, Sicheng Fan. Thanks for all the good times we spend together and it would definitely be existing in my memory forever.

My sincere thanks to the staff in the nanoFAB at the University of Alberta (Scott Munro, Aaron Hrycuw, Shiau-Yin Wu, Les Schowalter) for training me on various equipment which are essential for my research. I want to extend my thanks to everyone working in Preciseley Microtechnology Inc. (Lawrence Lam, Tongling Wang, Tiansheng Zhou) for everything I have learned and thanks for the forgiveness

Contents

List of Figures

List of Tables

List of Symbols

V_{oc}	Open circuit voltage
I_{sc}	Short circuit current
η	Fill factor
n	Refractive index
γ	Angle of emission cone
$d_{np\text{-}np}$	The distance between adjacent nanopillars
W_{CQD}	The width of the depletion layer
L	Carrier diffusion length
β	The SPP propagation constant on metal surface
k_0	Wavenumber of light in free space
ε_d	Permittivity of dielectric materials
ε_m	Permittivity of metallic materials
k_B	Wavenumber of the 1D grating
θ	Incident angle
Λ	Grating constant
a	The distance between adjacent cavities
P_g	The total power absorbed by the cell with grating structure
P_r	The power absorbed in flat structure

List of Abbreviations

CCE   carrier collection efficiency

c-Si   crystalline silicon

DBH   depleted bulk heterojunction

EBPVD   electron beam physical vapor deposition

EBL   electron beam lithography

EF   enhancement factor

EM   electromagnetic

EQE   external quantum efficiency

E-field   electrical field

FDTD   finite-difference time-domain

FF   fill factor

ICP   inductively couple plasma

ITO   indium tin oxide

LSP   localized surface plasmon

LTS   light trapping structure

MIM   metal-insulator-metal

NIL   nanoimprint lithography

NSL   nanosphere lithography

PbS CQD   lead sulfide colloidal quantum dot

PCE   power conversion efficiency

PML   perfect match layer

PV   photovoltaic

PVD	physical vapor deposition
P-NIL	photo assisted transfer nanoimprint lithography
QD	quantum dot
RIE	reactive ion etching
SEM	Scanning electron microscope
SERS	surface enhanced Raman scattering
STEM	Scanning transmission electron microscope
SPP	Surface plasmon polariton
SP	surface plasmon
T-NIL	thermoplastic transfer nanoimprint lithography
1D	one-dimensional
2D	two-dimensional
Cr	Chromium
Ag	Silver
Al	Aluminium
Au	Gold
SiO2	silicon dioxide
TiO_2	Titanium dioxide
GaAs	Gallium arsenide

Chapter 1. Introduction

The thesis concentrates on the study of the light trapping structures for PbS colloidal quantum dot (CQD) photovoltaic (PV) cells to improve the energy harvest efficiency of the device with both simulation and experimental approaches. PbS CQD cells have emerged as a new member of the photovoltaics family in the pasting decade, which shows great advantages for its easy fabrication process and potentially low-cost manufacturing.[1] However, the PCE for PbS CQD cells is still relatively low, holding it back from real-world applications. On the other hand, light trapping technique, as a reliable way to increase PCE of PV cells, has attracted wide attentions as lots of novel thin film solar cells being successfully demonstrated recently.[2-9] This chapter will illustrate the basic working principle of light trapping assisted PV cells and various fabrication methods for light trapping structures. Moreover, the previous research of light trapping structure on PbS CQD cells will be summarized. In the end of this chapter, the rationale of the thesis will be presented.

1.1   Solar cell and light trapping

Since the second industrial revolution, our demand for electricity is growing over the time, from the conventional electricity powered factories to electrical automobiles in the future. Although electric motors and appliances as clean technologies are gradually taking the place of combustion engines from every aspect of life, today the majority of electricity is still generated by consuming the fossil fuels like coal and gas and the renewable electrical generation only takes up to 25% of gross electricity generation until 2011.[10] In the foreseeable future, there will be an increase of electricity consumption due to the popularity of industrial robots and electrical vehicles and cut-down of traditional fuels usage for deteriorating

environmental issues. It was predicted by Hoffert et al.[11] that the globe energy demand will reach 27 terawatts by 2050 and a terawatts scale solar energy capacity is needed to cover the energy gap. However, there are two main problems preventing photovoltaics to move a huge step forward to become a noticeable and reliable energy source: the high production cost of conventional crystalline silicon (c-Si) solar cells and comparable lower PCE for novel thin film solar cells. Fortunately, science and technology can always find its way to push the boundary forward and solve various challenges. Numerous researches have been done in the past few decades to increase the PCE and reduce cost at the same time, and light trapping technique is one of these efforts.[6, 12-14] The basic idea of light trapping, as is named, is to confine the light energy inside the solar cell by special engineering designs so that more energy can be absorbed within limited thickness of light absorbing materials. As a result, light trapping is of vital importance for the thin film solar cells which usually have very thin active layer and poor light absorption capability. Assisted by the fast developing nanofabrication techniques, the light trapping has developed into a mature technique which is more controllable and repeatable. The following subchapters will provide a brief introduction on the basic principle of the PV cells and the light trapping techniques.

1.1.1 Working principle of PV cells

The typical structure of thin-film PV devices is shown in Figure 1.1 (a) and in most cases, it is made of 4 stacked layers. The layer 1 is the front transparent electrode from which the light enters into the device. The transparent conductive oxide glass, such as ITO, is usually used for that purpose due to its high conductivity and transparency in visible and near infrared range. Layer 2 is a n-type semiconductor material. Layer 3 is p-type material and makes a p-n junction with the layer 2. The depletion region can be generated close to the interface between layer 2 and 3 which

is the most important part of the PV cells. Layer 4 is the back reflection electrode which is usually made of metal. For most solar cells, the active layer is the sum of layer 2 and layer 3, which absorb photons and generate electrons and holes as shown in Figure 1.1 (b). When light enters into the active layer of the device, the photon with higher energy than the bandgap of the absorption material will be absorbed to generate electron-hole pairs. These electron-hole pairs generated inside the depletion layer of the p-n junction get separated under the internal electrical field (E-field) and move to opposite electrodes respectively. If the two electrodes are connected, the separated electrons and holes get recombined through the external circuit under the electrical force and generate current. For the open circuit case, the carriers accumulate and remain on the electrode until the E-field between the electrodes are large enough to neutralize the internal E-field of the p-n junction.
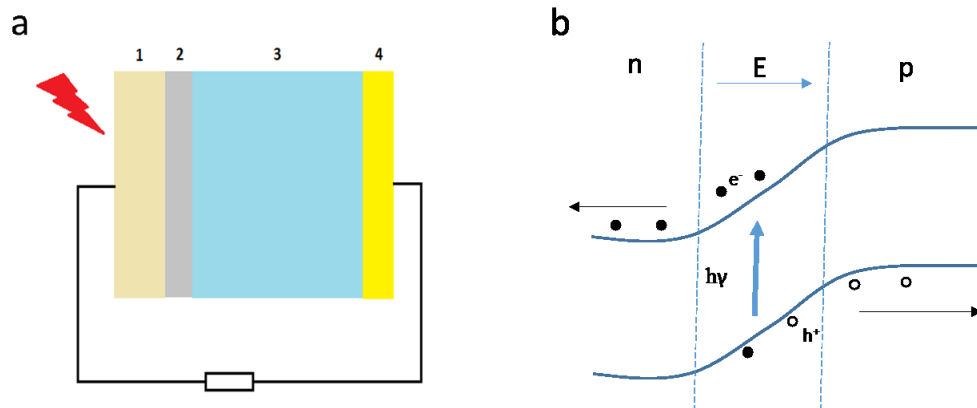
Figure 1.1 (a) the typical schematic of the photovoltaics devices. (b) The common p-n junction band structure in PV cells.

The maximum power output of the solar cells is expressed by:

$$P_{out} = \eta V_{oc} I_{sc} \qquad (1.1)$$

Here, V_{oc} is the open circuit voltage, I_{sc} is the short circuit current, and η is fill factor (FF) of the device. According to a simple picture, V_{oc} is mainly determined by the intrinsic material and electrical property and the physical architecture of the device. On the other hand, the I_{sc}, which equals the amount of the carriers passing the external

3

circuit during unit time, is closely related to the external quantum efficiency (EQE) of the device. The FF is a calculation result from the experimental tests which does not have specific physical meaning.

Due to the scaling effect of the c-Si PVs, the price of solar cells per watt has been largely reduced in the past few decades and the price of c-Si solar cell today is mainly subject to the cost of high purity crystalline Si. As a result, in order to get cheaper PVs, thin film solar cells becomes an excellent option as the thickness of thin film solar cells is normally less than 10 um,[15] which can save huge amount of light absorption materials compared with c-Si PVs. Thin film PVs can be made from both inorganic materials like gallium arsenide (GaAs), PbS quantum dots (QD), organic materials and hybrid organic-inorganic materials. Moreover, the tandem thin film PVs make it possible to make high efficiency cells that cover the wavelength range from visible to near infrared to make full use of the solar spectrum. For emerging PV techniques, ultrathin films (< 1um) are used for absorbing light. These ultrathin film PV cells have a primary drawback that the near-bandgap light absorption is small due to the limitation of active layer thickness. It is difficult to have all the photons with energy beyond the bandgap thoroughly absorbed in a several hundred nanometer active layer. Meanwhile, the carrier collection efficiency (CCE) would decrease if the thickness of active layer increased due to the low carrier mobility and short carrier life time inside the absorbing material. Thus, there is a trade-off between the light absorbance and the carrier transport, and emerging PV techniques with ultrathin films need optimization to achieved largest output power. That is an important barrier that limits the performance of ultrathin film PVs. The light trapping gives a perfect solution to the problem from two aspects: 1) the light trapping can largely increase the effective traveling path of light inside the active layer and more energy can be absorbed; 2) the depleted bulk heterojunction (DBH) can be formed and will increase the carrier collection efficiency inside solar cells.

1.1.2 Light trapping structures in PVs

The light trapping for PVs has passed through a long process of development. The early experimental works for the light trapping research date back to 1980s by Goetzberger. A.[16] on c-Si cells with a diffusive back reflector. The textures are random and the dimension of the structures are about few micrometers. Light trapping in such devices is caused by the light scattering and randomly reflection between the electrodes. With the advancement of nanofabrication techniques, the structures used for light trapping has evolved from the random textures to more regular and periodic photonics structures. The photonic structures are able to scatter and diffract light more efficiently and subsequently increase the light trapping capability. Most of all, with periodic structures, it became possible to control and adjust the light trapping wavelength and make optimization for different PVs. In the past decade, the fast development of SP structures had also accelerate the application of light trapping in PVs and other optoelectronics devices. Despite strong scattering of plasmonic structures, it can also increase the E-field intensity near the metal surface by the excitation of SP.

Light trapping achieved with dielectric patterns is still the most reliable and efficient method to enhance the PV performance. Early light trapping solar cells used the random textures at the interface between dielectric layers as shown in Figure 1.2 (b). Compared with plane interface (Figure 1.2 (a)), random propagation enables the light to travel a longer distance inside the active layer and hence leads to absorption enhancement. The light trapping is quantified with a parameter 'enhancement factor' (EF) which is defined by the average light traveling path inside active layer with light trapping over that value without light trapping structures. For the optical thick active layers, the EF has been proven to have an upper limitation of $2n^2/sin^2\gamma$ based on ray optics calculation.[17] Here, n is the refractive index of the material and γ is the angle

of emission cone in the surrounding medium. However, when the thickness of the absorption layer decrease to light wavelength scale, the EF can exceed the limitation with the application of periodic structure (Figure 1.2 (c)) due to the breakdown of ray optics theory at the nanoscale.[18, 19] One of the most famous work about light trapping is the demonstration of Si nanowire solar cell by E. Garnett *et al.*[8] The 2D nanowire array is fabricated with NSL and the calculated EF of 73 was achieved. Except for the light trapping effects, the periodical structures inside the active layer can sometimes also help to increase the charge collection efficiency due to enlarged contact area of the electrode, for instance using dye-sensitized solar cells.
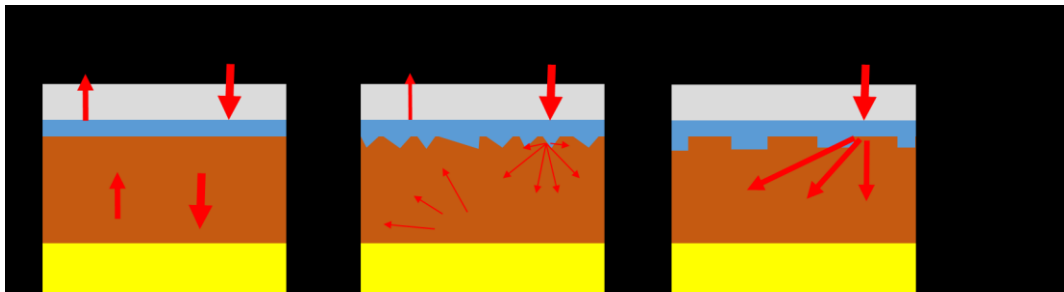
Figure 1.2 (a) The solar cell with plane electrode, light double pass the active layer and reflected back. (b) The solar cell with random roughness front electrode, light scattered and travels in different direction inside the solar cell. (c) The solar cell with periodic patterned electrode. Light can be diffracted into different orders and enhancement factor can be quite high for certain wavelengths.

The research of thin film plasmonic PVs have overwhelmed the light trapping dielectric material in recent years. The plasmonic structures are essentially metallic structure which can generate SP. Those metallic structures have shown wide applications in various fields and the application in PVs is one of them. Different from dielectric structures, the metallic structures scatters light by the excitation of SP resonance which can be explained as strong electron and external electrical field interference. Metal particles has tens of times scattering cross section than the dielectric particle of the same size. The advantage of high scattering efficiency allows the plasmonic particles to be doped in the active layer and caused minimum impact to device. Atwater[7] has summarized the application of plasmonic structures in solar

6

cells into three approaches as shown in Figure 1.3. In Figure 1.3 (a), metallic particles are placed on the surface of solar cell. Light trapping is achieved by the high front scattering efficiency with large scattering angle and multiple reflection and scattering to increase the effective optical path length in the cell. Additionally, metallic particles can be also doped into the cell active layer as shown in Figure 1.3 (b), and excitation of SP resonance can increase the energy absorbed per unit volume of absorption material by enhanced near field light intensity. Moreover, periodic metallic grating can be used as back reflector (Figure 1.3 (c)) which is similar to dialectical grating, which can cause light diffraction and meanwhile, concentrate light with SP excitation. Several plasmonic organic thin film PV cells and quantum dots PV cells have been demonstrated recently and remarkable efficiency has been achieved. [7]
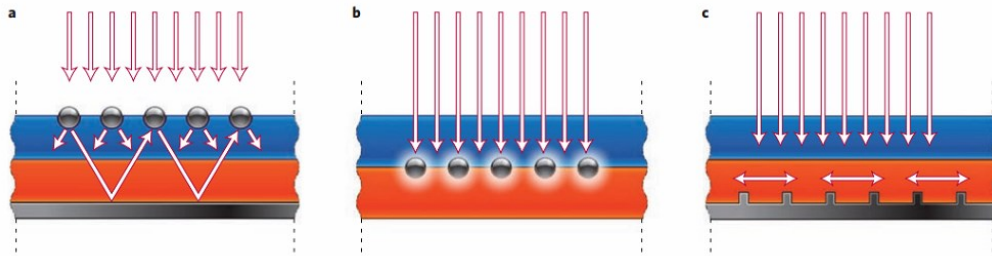
Figure 1.3 (a) The metallic nanoparticles placed on the top of the PV cells as scattering centers to increase the light traveling path. (b) The nanoparticles doped inside the active layer as nanoantennas to concentrate light and increase in-layer E-field intensity. (c) The patterned back metallic reflector which can couple the incident light to the surface plasmon polariton and confine the energy at the metallic-dielectric interface. Reprinted with permission from [7].

In this thesis, we will mainly discuss about the utilization of periodic structures as light trapping structures in the PVs, though most PVs today still employ random texture interface for easier fabrication process. It is believed that periodic structure is the first option for the future solar cells for its potential to be adapted for different light trapping applications.

1.2 Light trapping in thin film PbS CQD solar cell

The PbS QDs is a cheap and easy-accessible material which can be used for solar energy harvest. The PbS QDs can achieve a broad-band absorption by changing the quantum dot size and the PbS CQD solar cell of about 11.3% PCE has been fabricated to date.[20] However, the low power conversion efficiency of the PbS-CQD solar cells has been the bottle neck that forbids the utilization of PbS solar cell. The problem is mainly caused by the low carrier mobility and existence of defects inside the PbS CQD film fabricated by solution process. Although the carrier mobility and the film quality has been greatly improved in the past decade, the thickness of the PbS-CQD film is still only a few hundred nanometers which is insufficient for thorough absorption of photons near the band gap. As a result, light trapping structure (LTS) has been adopted in researches to mitigate the absorption-carrier collection trade-off in CQD PVs.

The initial attempts of the light trapping in PbS-CQD PVs appears in the DBH PbS CQD devices.[21, 22] The concept of the DBH is in contrast to the planar depleted heterojunction, and the bulk region of DBH consists of the mixture of the p-type and n-type materials instead of plane p-type and n-type layers, which is similar to the bulk heterojunction in the organic solar cells. The schematic allows the photon generated holes and electron separation occurs through the whole bulk region and the carriers can travel a shooter distance to leave the depletion region and reach the electrodes even for a thick absorption laye, avoiding a mass of recombination occurs inside the thick planar junction. For the PbS-CQD PV cells, the DBH consist of quantum dots and Titanium dioxide (TiO_2) nanoparticles or the ZnO nanowires have been successfully demonstrated.[21, 22] Aside from the influence on carrier collection, the randomly distributed nanostructures inside the active layer also act as light scatters and achieve light trapping. However, the dimension of nanostructures

gives a challenge to the thorough mixture of materials. Islands and voids can exist in such BDH with random nanostructures, compromising the advantages of the configuration. Figure 1.4 shows the improved DBH consist of periodic nanopillar structures by I. J. Kramer *al et*.[23] There is a calculated distance between adjacent nanopillars to efficiently collect the carriers expressed as:

$$d_{np-np} \approx 2 \cdot (W_{CQD} + L) \qquad (1.2)$$

Here $d_{np\text{-}np}$ is the distance between adjacent nanopillars, W_{CQD} is the width of the depletion layer in CQD layer and L is the carrier diffusion length. However, since the nanopillar dimension is optimized for carrier collection, the size of nanopillar is not large enough to cause noticeable light absorption enhancement.
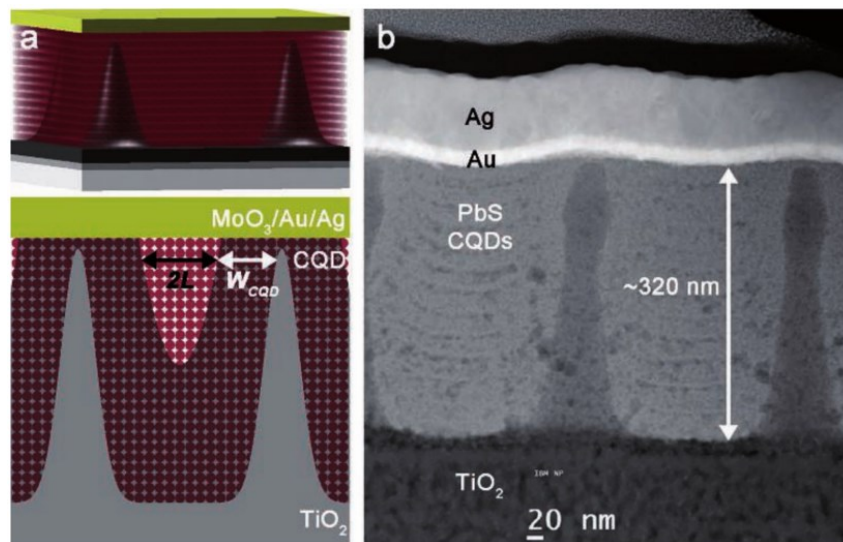
Figure 1.4 (a) Schematic and (b) scanning transmission electron microscope (STEM) image of the fabricated DBH PbS CQD solar cells. Individual layers of CQD formed by layer-by-layer process and the separation between TiO2 pillar and back electrode are evident. Reprinted with permission from [23].

Recently, optically optimized electrodes used for broad band PbS CQD solar cells has been successfully demonstrated by Adachi.[24] The configuration of the device is shown in Figure 1.5 (a). Both the front and the back electrode are periodically patterned with NSL and the patterns are hexagonal array. PbS CQD layer is sandwiched between the electrodes conformally. By comparing the simulation

results shown in Figure 1.5 (b) and 1.5 (c), great absorption enhancement was observed near the gold (Au) pillar structure due to the excitation of SP. Meanwhile, the patterned ITO electrode also plays a role in the overall light trapping effect. With such design, 31% improvement in short circuit current has been achieved compared with the solar cell with same PbS CQD quantity, leading to a 13.3% overall PCE improvement. Aside from this research, a very detailed study about the impact of patterned ITO electrode on PbS CQD PVs was conducted by S. M. Mahpeykar,[25] in which the light diffraction mode under different periodic ITO structure was investigated.
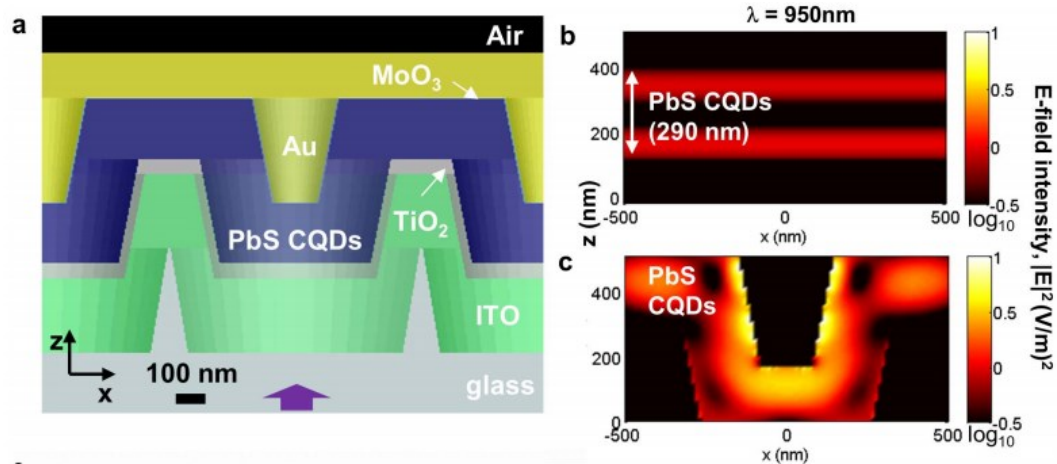
Figure 1.5 (a) The cross section illustration of a 3D hexagonal array of nanostructured CQD solar cells. The E-field intensity was simulated for (b) planar device and (c) patterned device respectively. Reprinted with permission from [24].

Except for the integration of periodic structure with PbS CQD PVs, the nanostructures with small dimension can be also doped into the active layer as light scatters. This research area is current under fast development with the research on light concentration effect of using metallic particles. The plasmonic PbS CQD cells doped with Au nanoshell has been successfully demonstrated by D. P-Soldan *et al.* in 2013.[26] The nanoshells was selected for its tunable localized surface plasmon (LSP) resonant wavelength due to hybridization of its internal and external LSP mode. The device schematic is shown in Figure 1.6. The nanoshell dimension is optimized

based on the required resonant wavelength and the refractive index of the surrounding PbS CQD layer. Additionally, a thin insolation layer is coated on the nanoshells to avoid the carrier combinations at the metallic particle surface. As is well known, metal can absorb light. Thus, it is critical to utilize the nanostructures with large scattering cross section and small absorption cross section in plasmonic PVs. However, there is still a long way to go for the wide application of plasmonic solar cell in view of the difficulties for the synthesis of specific metallic nanostructure and design of corresponding solar cell structure.
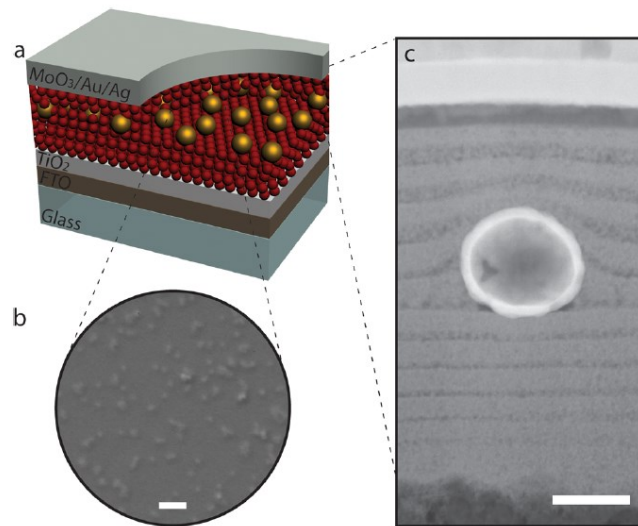
Figure 1.6 PbS CQD plasmonic solar cell device. (a) Schematic of the device with embedded nanoshells in PbS-CQD active layer. (b) Top view scanning electron microscope (SEM) image of the CQD film with nanoshells inside. (c) Cross section STEM showing a single Au nanoshells embedded in a PbS CQD film. Scale bar 100nm. Reprinted with permission from [26].

1.3   Periodical nanostructure fabrication method

Nanolithography is the key process in the microprocessor industry and hence get fast development in the past decades. The fabrication of LTS has also gotten a great step forward along with the advancement of nanolithography. However, as we know, photolithography is the main approach used in the semiconductor industry to fabricate nanoscale transistor for the microprocessors, but it was barely used for the

fabrication of LTS because of the high cost and low throughput. Thus, the time and cost are the main concerns for the fabrication of large-area LTS, which is also the motivation for the research of LTS fabrication. In this thesis, we will focus on the periodic LTS that help to increase the solar cell performance and hence, the common lithography techniques for periodic structure fabrication will be introduced in this chapter.

1.3.1 Electron beam lithography

The electron beam lithography (EBL) is a method using the focused electron beams to write the designed patterns directly on the substrate covered with electron resist and then turn written shape into nanoscale structures.[27] In general, the EBL process has three steps. First, the substrate covered with resist film is selectively exposed in the focused electron beam and then immersed in solvent to remove the exposed part. Then, the material is deposited on the substrate with physical vapor deposition. Finally, the substrate is immersed in the other solvent to remove the whole resist layer. The material deposited on resist layer will be removed simultaneously at the same time, left the written shape structure on the substrate. The EBL is a good way to generate periodic patterns with high precision (<10nm line width) and complexity, but its disadvantage is also obvious: the slow pattern writing process. Thus, for large area fabrication of periodic structures, EBL is not the first choice, especially when more convenient fabrication methods were developed recent years.

1.3.2 Nanosphere lithography

NSL is a very efficient way for two-dimensional periodic pattern fabrication developed at the end of last century by J. C. Hulteen *et al.*[28] The method utilizes the self-assembled polystyrene nanosphere with several hundred nanometer diameter

to form a closely packed monolayer mask. The nanosphere mask can be directly formed on the substrate or generated somewhere else and then transferred to the substrate as fabrication mask. Various structures can be fabricated, such as nanowire, nanopillar, nanotriangle, nanovoid etc, depending on different fabrication methods. Meanwhile, nanosphere mask is compatible with both bottom-up and top-down fabrication processes. Recently, the advancement of NSL is mainly reflected on the method to get self-assembled nanosphere mask with improved repeatability and pattern quality. Generally speaking, NSL is the most convenient method to obtain large area high quality periodic patterns with low cost.

1.3.3 Nanoimprint lithography

Nanoimprint lithography (NIL) is another high efficiency, low cost lithography approach developed by Fischer *et al.*[29] and the technique is most likely to be commercialized for the fabrication of large scale nanostructures in the future.[30-33] Similar to the optical lithography, the NIL requires the mold for the print instead of a mask and the complementary shapes of the mold can be generated on the substrate. There are several methods to transfer the patterns on the mold to the substrate: the thermoplastic transfer (T-NIL), photo assisted transfer (P-NIL). A layer of resist will be firstly deposited on the substrate before patterning and the resist will deform under certain conditions such as glass transition temperature or UV photons radiation. Then, the mold attached to the resist will be pressed into the resist. Afterward, the mold will be physically separated from the resist, leaving the patterns on the substrate. The nanoimprint for the 6 inch wafer scale has been realized recently,[32] representing another huge step forward in the field. However, The NIL has very high requirements on equipment and mold during the fabrication, making it unpopular for the scientific research. In addition, NIL is also facing challenges such as printing defects induced by the air bubbles and the mold wear under high temperature.

1.4 Outline of the thesis

In this thesis, we focus on the fabrication of 2D structures of both metal and dielectrics and investigate the light matter interaction on the fabricated structures for its potential application in PbS CQD solar cell. A comprehensive study is made from both simulation and experimental works.

Chapter 1 introduces the basic working principle of PV cells, light trapping schematics and the recent progress on the enhanced PbS-CQD solar cells with LTS. Additionally, the fabrication methods of the LTS have been briefly discussed.

Chapter 2 describes the experimental fabrication of the 2D hexagonal structures with NSL. A nanosphere mask fabrication method by self-assembling nanospheres at water-air interface is provided. The whole process to make 2D structures has been demonstrated and optimized for the large area 2D pattern which can be used in the thin film solar cell as the electrode.

Chapter 3 studies the SP modes observed on the fabricated 2D hexagonal silver gratings. Different excitation modes and mode hybridization are observed and analyzed with the FDTD simulation. Moreover, a comparison is made between the metallic grating and dielectric grating to figure out the difference in various SP modes.

Chapter 4 shows the application of large area 2D nanopillar and nanocavity structure in PbS CQD solar cells. A method to fabricate large area patterned ITO electrode is presented. The absorption enhancement in the PbS CQD cell is numerically investigated and the great light absorption enhancement is achieved with the assistant of the 2D LTS.

Chapter 5 summaries the works done in chapter 2 to 4. The future works required to improve the performance of PbS CQD solar cells are also briefly discussed.

Reference

1.   McDonald, S.A., et al., *Solution-processed PbS quantum dot infrared photodetectors and photovoltaics.* Nat Mater, 2005. **4**(2): p. 138-142.

2.   Ferry, V.E., et al., *Light trapping in ultrathin plasmonic solar cells.* Optics Express, 2010. **18**(S2): p. A237-A245.

3.   Müller, J., et al., *TCO and light trapping in silicon thin film solar cells.* Solar Energy, 2004. **77**(6): p. 917-930.

4.   Law, M., et al., *Nanowire dye-sensitized solar cells.* Nat Mater, 2005. **4**(6): p. 455-459.

5.   Anna Selvan, J.A., et al., *A new light trapping TCO for nc-Si:H solar cells.* Solar Energy Materials and Solar Cells, 2006. **90**(18–19): p. 3371-3376.

6.   Zhou, D. and R. Biswas, *Photonic crystal enhanced light-trapping in thin film solar cells.* Journal of Applied Physics, 2008. **103**(9): p. 093102.

7.   Atwater, H.A. and A. Polman, *Plasmonics for improved photovoltaic devices.* Nat Mater, 2010. **9**(3): p. 205-213.

8.   Garnett, E. and P. Yang, *Light Trapping in Silicon Nanowire Solar Cells.* Nano Letters, 2010. **10**(3): p. 1082-1087.

9.   Yafei, Z., et al., *Development of Inorganic Solar Cells by Nanotechnology.* Nano-Micro Letters, 2012. **4**(2): p. 124-134.

10.   OECD, *Electricity generation*. OECD Publishing.

11.   Hoffert, M.I., et al., *Energy implications of future stabilization of atmospheric CO2 content.* Nature, 1998. **395**(6705): p. 881-884.

12.   Callahan, D.M., J.N. Munday, and H.A. Atwater, *Solar Cell Light Trapping beyond the Ray Optic Limit.* Nano Letters, 2012. **12**(1): p. 214-218.

13.   Campbell, P. and M.A. Green, *Light trapping properties of pyramidally textured surfaces.* Journal of Applied Physics, 1987. **62**(1): p. 243-249.

14.   Teck Kong, C., et al., *Optimal wavelength scale diffraction gratings for light trapping in solar cells.* Journal of Optics, 2012. **14**(2): p. 024012.

15.   Aberle, A.G., *Thin-film solar cells.* Thin Solid Films, 2009. **517**(17): p. 4706-4710.

16.   Goetzberger, A., *Optical confinement in thin Si solar cells by diffuse back reflectors*, in *15th Photovoltaic Specialists Conference*. 1981: Kissimmee, FL. p. 867-870.

17.   Yablonovitch, E., *Statistical ray optics.* Journal of the Optical Society of America, 1982. **72**(7): p. 899-907.

18.   Battaglia, C., et al., *Light Trapping in Solar Cells: Can Periodic Beat Random?* ACS Nano, 2012. **6**(3): p. 2790-2797.

19.   Yu, Z., A. Raman, and S. Fan, *Fundamental limit of nanophotonic light trapping in solar cells.* Proceedings of the National Academy of Sciences, 2010. **107**(41): p. 17491-17496.

20.   National Center for Photovoltaics. *Research Cell Efficiency Records*. 2016; Available from: http://www.nrel.gov/ncpv/.

21.   Jean, J., et al., *ZnO Nanowire Arrays for Enhanced Photocurrent in PbS Quantum Dot Solar Cells.* Advanced Materials, 2013. **25**(20): p. 2790-2796.

22.   Barkhouse, D.A.R., et al., *Depleted Bulk Heterojunction Colloidal Quantum Dot Photovoltaics.* Advanced Materials, 2011. **23**(28): p. 3134-3138.

23.   Kramer, I.J., et al., *Ordered Nanopillar Structured Electrodes for Depleted Bulk Heterojunction Colloidal Quantum Dot Solar Cells.* Advanced Materials, 2012. **24**(17): p. 2315-2319.

24.   Adachi, M.M., et al., *Broadband solar absorption enhancement via periodic nanostructuring of electrodes.* Scientific Reports, 2013. **3**: p. 2928.

25.   Mahpeykar, S.M., Q. Xiong, and X. Wang, *Resonance-induced absorption enhancement in colloidal quantum dot solar cells using nanostructured electrodes.* Optics Express, 2014. **22**(S6): p. A1576-A1588.

26.   Paz-Soldan, D., et al., *Jointly Tuned Plasmonic–Excitonic Photovoltaics Using Nanoshells.* Nano Letters, 2013. **13**(4): p. 1502-1508.

27.   Vieu, C., et al., *Electron beam lithography: resolution limits and applications.* Applied Surface Science, 2000. **164**(1–4): p. 111-117.

28.   Hulteen, J.C. and R.P. Van Duyne, *Nanosphere lithography: A materials general fabrication process for periodic particle array surfaces.* Journal of Vacuum Science & Technology A, 1995. **13**(3): p. 1553-1558.

29.   Fischer, U.C. and H.P. Zingsheim, *Submicroscopic pattern replication with visible light.* Journal of Vacuum Science & Technology, 1981. **19**(4): p. 881-885.

30.   Battaglia, C., et al., *Nanomoulding of transparent zinc oxide electrodes for efficient light trapping in solar cells.* Nat Photon, 2011. **5**(9): p. 535-538.

31.   Ji, R., et al., *UV enhanced substrate conformal imprint lithography (UV-SCIL) technique for photonic crystals patterning in LED manufacturing.* Microelectronic Engineering, 2010. **87**(5–8): p. 963-967.

32.   Hornung, M., et al. *6 inch full field wafer size nanoimprint lithography for photonic crystals patterning.* in *Nanotechnology (IEEE-NANO), 2010 10th IEEE Conference on.* 2010.

33.   Kang, M.-G., et al., *Organic Solar Cells Using Nanoimprinted Transparent Metal Electrodes.* Advanced Materials, 2008. **20**(23): p. 4408-4413.

Chapter 2. Fabrication of 2D lattice with NSL

2.1 Introduction

Our world has become smaller nowadays. The advancement of techniques has bridged the distance of people and shrunk the stuff we used in the modern life. From the consumer electronic devices to the industry detectors, everything trends to be more complex and more powerful. However, all these changes rely on inventions in modern electronics, which would not work without the great advance in the nanoscience and lithography techniques. The nanolithography can be categorized into two kinds: "replication techniques" and "pattern generation techniques". The replication means to make the nanostructures out of the already made masks or molds with high throughput and low cost, but the technique cannot be used for the initial pattern preparation.[1-3] The patterning generation, on the contrast, refers to the technique used for the direct fabrication of nanostructures.[4-6] Some of the replication techniques has been mentioned in the chapter 1, such as the optical lithography and the nanoprinting lithography, and these techniques rely heavily on the quality and the size of the mold used in fabrication. Thus, the pattern generation is the most important part in the nanofabrication. However, the conventional nanoscale pattern generation methods like EBL have been challenged for the balance of the cost, precision and dimension.[7, 8] Therefore, patterning periodic nanoscale 2D arrays with simple unit cell is of interest in academic research for its potential applications in electronics and photonics.

NSL has recently attracted attentions for patterning periodic and large scale nanostructure, as it does not require expensive equipment and complicated

fabrication process.[9-12] Except for the fabrication of structures as mask or mold, NSL can be also regarded as a replication technique since the fabrication of nanosphere mask is simple and time saving. But, the nanoarrays fabricated by NSL so far are all hexagonal distribution due to the immutable nanosphere mask structure, limiting the broad application of NSL.

The process for a standard NSL contains three main steps, as shown in Figure 2.1. The nanosphere used for the lithography is mostly made of polymer with the size ranging from 100 nm to several micrometers. The method to arrange the nanosphere on the substrate to form a monolayer nanosphere mask can be varied. The first reported NSL by Fischer and Zingsheim in 1981 used a drop of nanosphere suspension to form the colloidal nanosphere mask on the substrate,[13] but the formed patterns had lots of defects. The quality of the nanosphere mask has direct influence on the uniformity of fabricated arrays and the shape of the structures. Thus, nanosphere mask fabrication is the most important step in NSL. In the high precision fabrications, the mask annealing step should be added to eliminate the movement of nanosphere after the mask fabrication.[14] When the original mask is ready, the mask can be further modified by shrinking or augmenting the size of spheres, leading to the separation or the aggregation of the nanospheres.[15] The mask modification should be properly designed for the fabrication of different structures. With the modified nanosphere masks, the final structure can be fabricated with the physical vapor deposition (PVD) and the reactive ion etching (RIE) process. The PVD can generate a structure layer on the top of the substrate and the RIE, on the other hand, directly etch the patterns on the substrate.
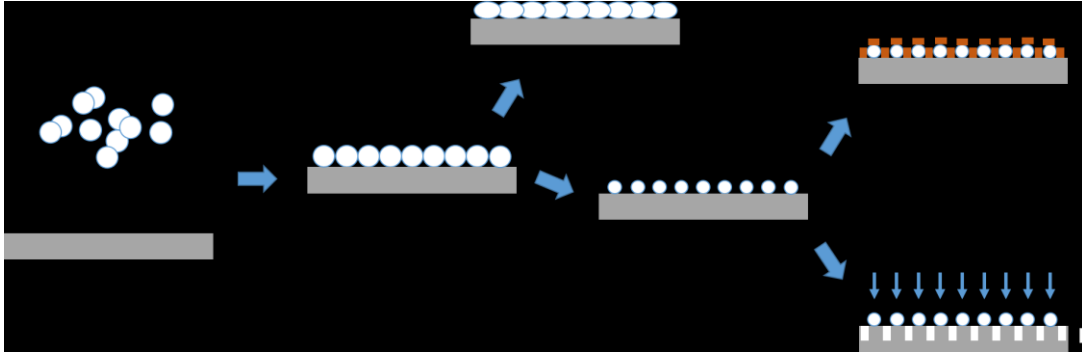
Figure 2.1 The general fabrication process for the NSL. Step 1: The fabrication of monolayer nanosphere mask. Step 2: The modification of fabricated mask. Step 3: patterning the substrate with PVD or RIE.

In the previous studies, the successfully fabricated structures with NSL include nanotriangle, nanodot nanopillar, nanocavities, and special structure such as nanoring and nanorod.[16-18] The nanotriangle array is the most common pattern fabricated with the NSL which has been widely used for surface enhanced Raman scattering (SERS) due to strong electromagnetic (EM) field intensity between the contiguous triangle points through LSP coupling.[19, 20] The generation of the nanopillars and the nanocavity array is by PVD and RIE which will be introduce in this chapter. Other nanostructures such as nanorod and the nanoring requires special deposition techniques with a tilting angle of the sample.

2.2 General nanosphere mask preparation methods

2.2.1 Spin coating

The spin coating technique is commonly used to form thin layers of materials in academic research.[9, 21] Under the centripetal force generated by the spindle, the liquids on the spin stage can be dispersed uniformly within very short time. The centripetal force can be controlled over the spin speed of the stage and the coated layer becomes thinner as the spin rate increases. The thickness of the deposition layer can be changed from <10 nm to several hundred nanometers. Similarly, the

nanosphere mask can be also fabricated with the spin coating process with the aid of the centripetal force as shown in Figure 2.2. The nanosphere suspension is firstly dropped on the substrate attached to the center of spin stage. The suspension drop should be left on the substrate for a while to let some nanosphere to be attached to the substrate. Then, turn on the spindle and accelerate to the set spin speed and keep the speed for a certain time to remove the redundant suspension on the substrate. During the spin, the suspension solvent and the nanospheres are under the centripetal force at the same time. When the solvent with larger density than polymer nanospheres is used, the solvent is under larger centripetal force and will push the nanospheres back to the center spin stage and form a closely packed nanosphere layer on the substrate. The factors that influence the final mask quality include the selected suspension, the suspension concentration, the spin rate and the waiting time. Too many variables make it hard to get a good control of the formed nanosphere mask.
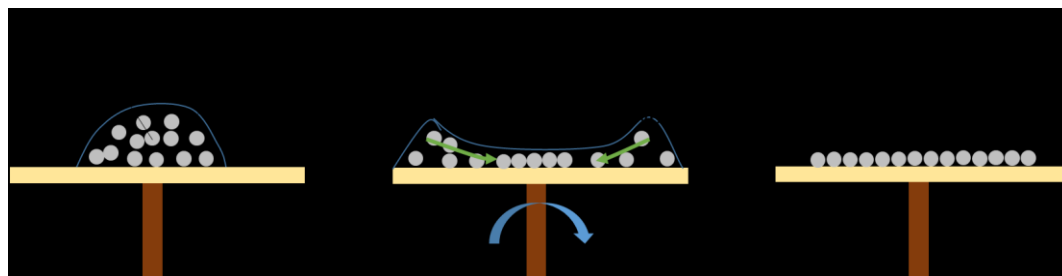
Figure 2.2 The fabrication of nanosphere mask with spin coating. The nanosphere suspension with proper suspension concentration is dropped at the center of the substrate which is placed on the spin coater.

2.2.2 Drop casting

The drop coating, which is also known as evaporation method for nanosphere mask fabrication and the process, is even simpler than the spin coating.[22] The nanosphere suspension is directly dropped on the substrate and then wait until the solvent get evaporated. When the concentration of the suspension is very low, a thin layer of nanospheres can be formed on the substrate and the nanospheres self-

organized into closely packed mask during the evaporation process. The drop casting is a quick approach to fabricate small size mask on the substrate and it is hard to fabricate high quality monolayer nanosphere masks due to poor controllability of the fabrication process.

2.2.3 Nanosphere self-assembly at the interface of two different media

The self-assembly of nanospheres at interface of two different media has been demonstrated for the fabrication of ultra large monolayer mask with high quality in previous studies.[11, 23] In this method, the interface of materials with different phases such as the air-water interface are used for the self-assembly. The nanospheres are carefully dispersed and trapped at the interface of materials with different phase and self-organized into a monolayer mask. The formed mask can be easily deposited on the substrate by removing the lower phase material. The method about how to spread the nanosphere at the interface is the most important part for this method and different approaches such as direct pipette dispersion, dispersion with slope or dispersion with dispersion stage have been successfully demonstrated.[10, 24] This NSL technique is the fabrication method we employed in our research and the detail process will be provided in the following subchapters.

2.3   2D periodic nanostructure fabrication with NSL

For the purpose of fabricating large area light trapping structures in our study, self-assembly of nanospheres at the water surface is applied to get controllable and repeatable nanostructures. Here, the detailed fabrication process and parameters applied in fabrication is discussed in this subchapter.

2.3.1 Fabrication of the nanosphere mask

Nanosphere mask fabrication with spin coating

The nanosphere suspension was prepared with 2:1 mixture of 10% w/w 500nm polystyrene nanosphere water suspension and Triton solution (Triton:Methanol=1:400). The 1 cm^2 glass substrate was used and placed at the center of the spin coater. The spin speed was set to 1500 r.p.m. for 15 s. Before spin, different waiting times was applied to wait for the nanospheres to attach to the substrate. The SEM image of the spin coating samples are shown in Figure 2.3 with different waiting times. The SEM images were obtained by a Ziess EVO scanning Electron Microscope.
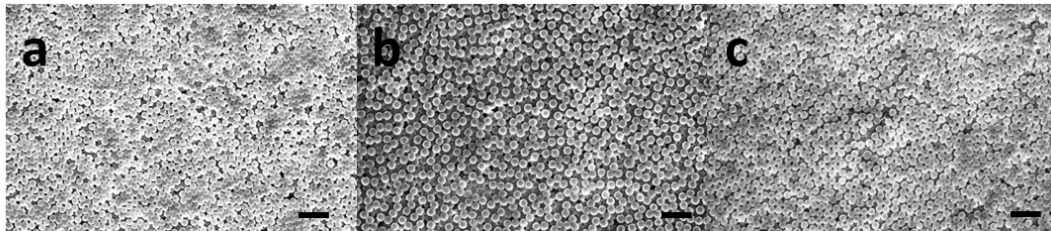
Figure 2.3 Nanosphere mask fabricated by spin process with the 1500 r.p.m for 15 s. (a) 15 s waiting time before spin. (b) 25 s waiting time. (c) 35 s waiting time. The scale bar is 2 um.

It is fairly difficult to obtain good patterns under the applied spin coating condition and the nanospheres are irregularly distributed with multiple layers of nanospheres. In the experiments, the increased waiting time only lead to increased amount of nanosphere layers. In summary, the spin coating method could be a good choice for the fabrication of 3D photonic crystal with multiple nanosphere layers. But, delicate control on the experiment condition is required to fabricate well defined monolayer nanosphere mask.

Mask fabrication with self-assembly of nanosphere at water surface

The self-assembly of nanospheres on the water surface also needs specifically prepared nanosphere suspension. For the 500 nm polystyrene nanosphere used in the

experiment, the 3.0% w/w nanosphere water suspension was mixed with Ethanol of the same volume. The nanosphere mask formation process is referred to the recent research by J. Yu *et al*.[24] To fabricate the nanosphere mask at the water/air interface, a carefully cleaned glass piece about 1 cm^2 was firstly placed inside a glass petri dish with 4 inch diameter as the nanosphere dispersion stage, which holds and spreads the nanosphere suspension to the water. Then, a few substrates, a bit thinner than the dispersion stage, were placed inside the petri dish. DI water was slowly added to the petri dish with a syringe to bring the water surface level 0.5 mm above the dispersion. Thus, the substrate surface is well below the water surface at the same time. Afterward, about 20 uL prepared nanosphere suspension was dropped on the dispersion stage. It was observed that the suspension spread and covered the whole dispersion stage, and the nanospheres left the stage and quickly spread at the water surface when reached the edge of the stage, assembling into 2D arrays. Most of the nanospheres remained at the water surface due to its low density and strong water surface tension. However, the nanospheres may also enter the water due to the collision between nanospheres. The suspension was constantly dropped on the glass stage until the nanosphere monolayer covered most of the water surface. The mask formation process is shown in Figure 2.4 (a) and 2.4 (b) and large area of monolayer mask can be observed at the water surface. Finally, the water inside the petri dish is slowly removed using a pipette and the disruption of the floating nanosphere mask should be avoided. As the water level lowered, the mask would be slowly deposition on the substrate. The substrate covered by the mask was then taken out from the petri dish when the surface dried.

The SEM images in Figure 2.4 (c) and 2.4 (d) show the fabricated mask deposited on the glass substrate. It is shown that very large single crystalline area can be formed with closely packed nanospheres. Some single nanosphere can be observed on the top of mask, which is due to the existence of the nanospheres inside

the water during the mask transfer process. However, it can be observed that most of the formed area are well-patterned single crystalline structure with low-density of defects in the structure.
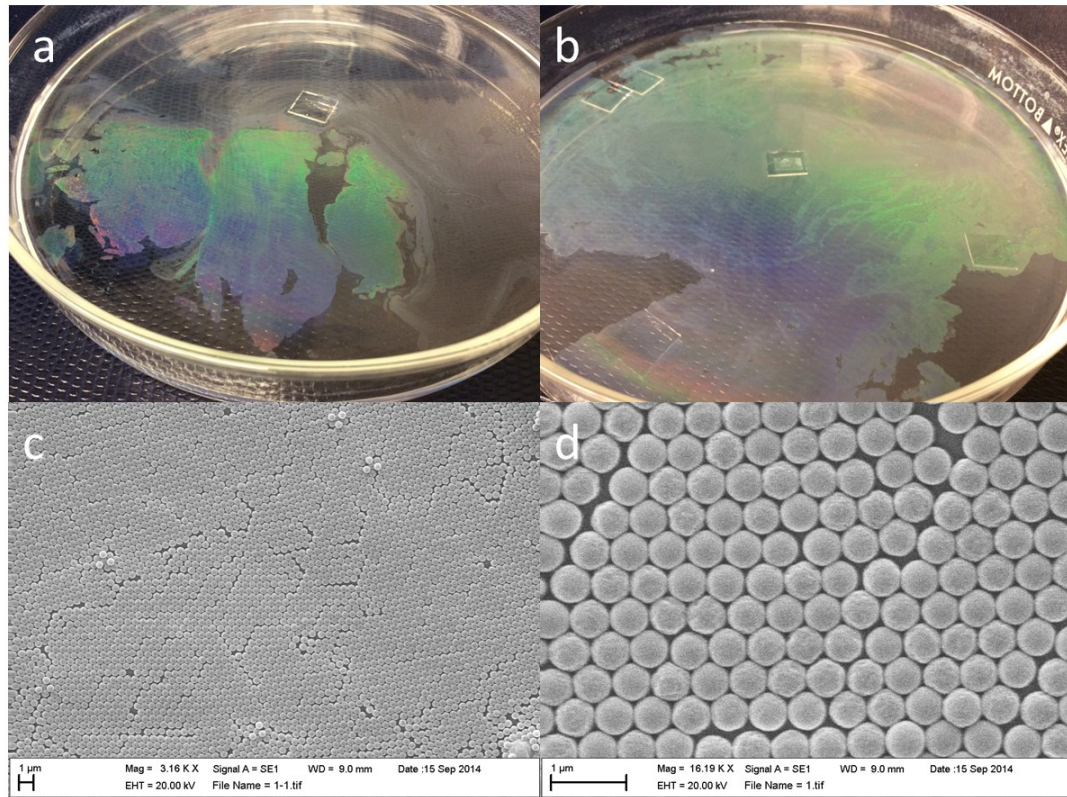
Figure 2.4 The formation of monolayer mask flowing on the water: (a) the nanospheres start to disperse at the water surface and (b) the nanosphere mask occupies the majority of water surface in the petri dish. (c) The SEM image of the fabricated nanosphere mask. (d) The zoom-in view of the closely packed nanospheres.

The distinguishment of regions with good quality and bad quality is important since it is hard to ensure the whole water surface is covered with well-patterned mask and we should make sure that high quality mask is transferred to the substrate. The conventional method using SEM to determine the good lattice quality region is time consuming and the samples under observation will be permanently damaged. To develop an easier approach to judge mask quality, areas with different appearance under naked eyes were measured using SEM, as shown in Figure 2.5. It is shown that the brightness of different areas on the substrate can be various due to the different

25

diffraction efficiency of patterns. The higher brightness areas trend to be of better crystal lattice quality. The darker area is likely to be formed with looser arranged nanospheres which has rather low diffraction efficiency. Additionally, the arrangement of nanosphere arrays is single crystalline if the color is shown to be uniform single color on the mask.
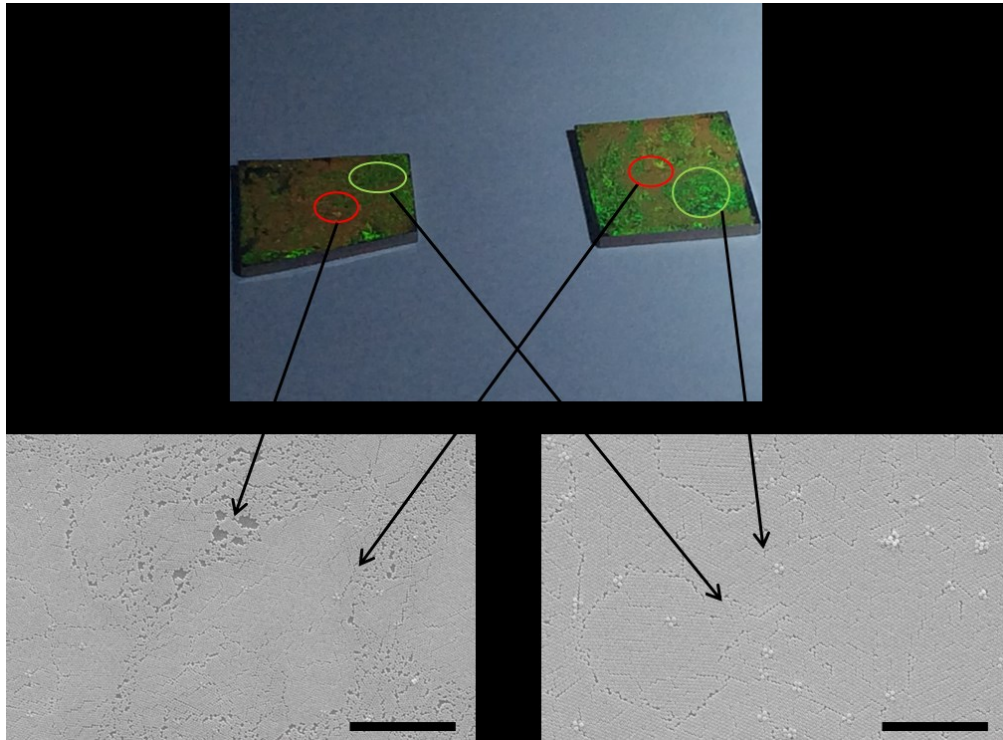
Figure 2.5 The comparison of different areas on the mask under the SEM. The brighter area shows better nanosphere mask quality than the darker area.

According to various experimental studies, it is found that the position of placed glass stage in the petri dish can strongly influence the overall quality of the mask. When the stage is placed at the center of the petri dish, the nanospheres will be spread from four directions as shown in Figure 2.6 (a). The nanospheres flowing on the water surface will reach the boundary of the petri dish within very short time and bounce back. The mixture of different nanosphere streams will cause collision between nanospheres, which deteriorate the quality of the nanosphere mask in two ways. Firstly, the collision force between different nanosphere streams will submerse

part of the nanospheres into the water and these submersed nanospheres are likely to form multilayers on the fabricated mask. On the other hand, the mixture of the nanosphere streams will destroy some of the already-patterned mask and break a larger single crystalline area into multi-crystalline area. According to our observation, the nanosphere dispersion process can be further optimized with designated nanosphere flowing direction by changing the dispersion stage position. When the stage is placed at the edge of the petri dish as shown Figure 2.6 (b), the different nanosphere streams can work in a constructive way. The proper choice of the position for the dispersion stage can greatly minimize fabrication time and increase the mask fabrication yield. For the high precision applications, the quality of masks can be further improved by a mask annealing step, which is used to avoid the deformation of mask duration water evaporation.[14, 24]
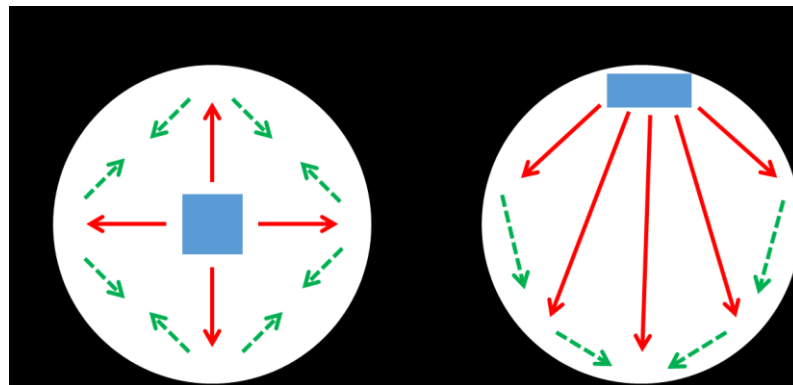
Figure 2.6 The movement of the nanosphere stream at the water surface when the glass dispersion stage (blue rectangle) is placed at (a) the center of the petri dish and (b) the edge of the petri dish. The red arrow indicate the stream flowing direction off the glass stage and the green arrow is the bounce direction of the nanosphere stream.

The nanosphere mask transfer from the water surface to the substrate is by simply removing the water below the floating mask. It is shown that the mask can be favorably transferred when the substrate is hydrophilic. However, there will be a problem if the mask is to be transferred to hydrophobic surface. It was observed that the water will escape from the hydrophobic surface such as Si surface and

polydimethylsiloxane (PDMS) surface quickly when the water level approaches the surface of the substrate, together with the self-assembled mask flowing on it. Therefore, no large area patterns can be left on such surface. In our study, the surface of the employed Si and PDMS substrates were treated with the oxygen plasma RIE. This process can relieve the aforementioned problem, since the RIE treatment can turn the hydrophobic surface of the material into hydrophilic.[25] For PDMS, the treated surface will turns back to hydrophobic after a certain time, depending on the RIE treatment time. With the assistant of RIE treatment, successful pattern transfer has been achieved on PDMS and Si substrates if the whole process is finished before the surface property turns back.

2.3.2 Nanosphere mask modification

The further mask modification of the original nanosphere mask is necessary to fabricate diverse nanostructure arrays. The mask modification can be divided into mask separation and fusion, which can be achieved by shrinking or augmenting the nanosphere size.

Polystyrene nanosphere size reduction

The sized of the polymer nanospheres can be reduced with the oxygen plasma RIE according to the previous studies.[26] The inductively coupled plasma (ICP) RIE system is used in our research since the more power plasma can be generated and thus more isotropic size reduction of nanosphere can be achieved. The main parameters in the RIE system include the source power, chuck power, the plasma flow rate, the etching duration. The injected gas is firstly ionized under the strong EM field and then flow into the etching chamber. The plasma move to the placed substrate under the driven EM field and react with the sample surface. In our study, the size of the etched nanospheres is controlled by adjusting the etching duration of the mask inside the RIE system. The SEM images of mask etched with different

etching duration are shown in Figure 2.7. 300 W source power, 20 W chunk power and 5 sccm (standard cubic centimeters per minute) oxygen flow rate are applied. It is shown that the shape of the etched nanospheres can become irregular when the size of the sphere is below 200 nm. This is because the sphere diameter decrease rate becomes much larger as the spheres become smaller, therefore the shape becomes more sensitive to the plasma gas distribution. Also, the uniformity of polymer nanospheres is another factor that affects the final shape. As a result, the smallest sphere used in our study is about 300 nm in diameter, in order to maintain spherical shape for nanospheres.
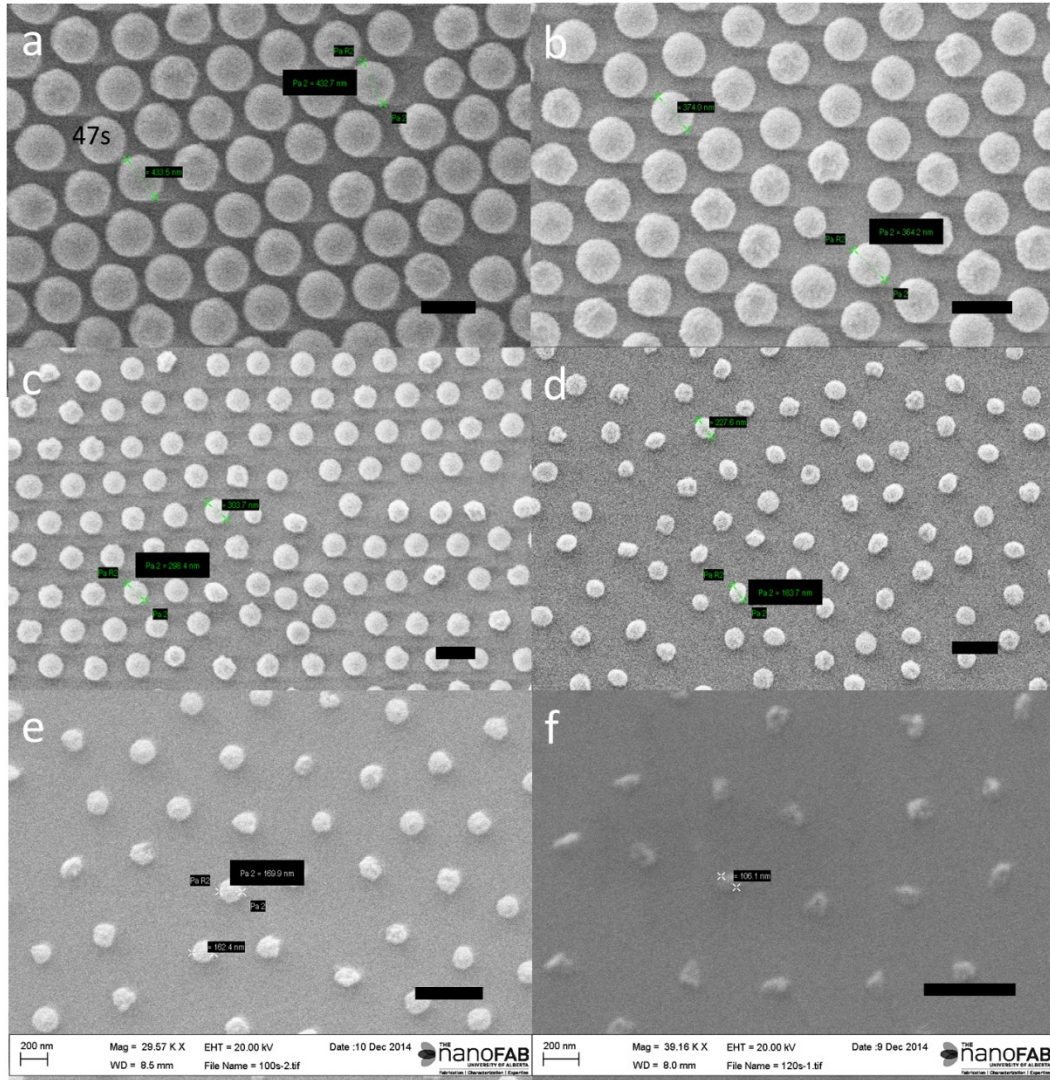
Figure 2.7 The SEM images of the polystyrene nanosphere mask modified with the oxygen RIE. The source power of 300 W and chunk power of 20 W are applied, and 5 sccm oxygen flow rate is used. Different RIE times are used for samples: (a) 47 s, (b) 62 s, (c) 72 s, (d) 82 s. (e) 100 s, (f) 120 s. The size of the nanospheres under test are marked. Scale bar indicates 500 nm for all samples.

The plot of yielding nanosphere size vs. etching duration is shown in Figure 2.8 (a) and Figure 2.8 (b). The RIE parameters are different for that two case. The parameter for Figure 2.8 (a) is with less flow rate but high chunk power than Figure 2.8 (b). It is shown that the diameter of the etched nanospheres decrease faster and larger discrepancy is presented for repeated process when large flow rate is applied. As a result, the RIE parameter for Figure 2.8 (a) is preferable due to the lower etching

30

rate which can enable us a better control on the nanosphere size.
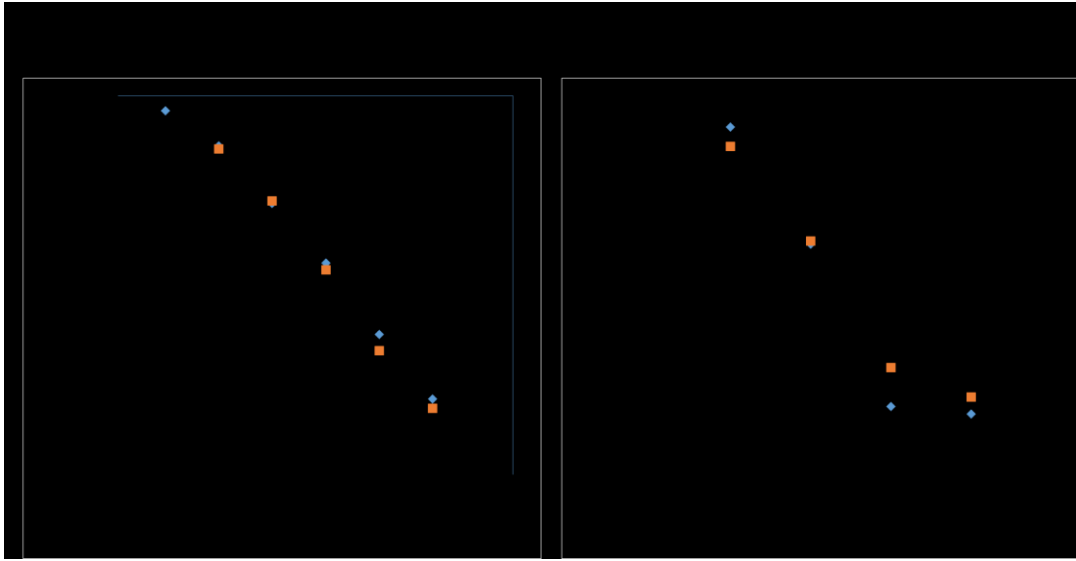
Figure 2.8 The nanosphere size as a function of the etching time with (a) 300 W source power, 20 W chunk power and 5 sccm oxygen flow rate and (b) 300 W source power, 10W chunk power and 30 sccm oxygen flow rate. The experiment was repeated for two times.

Polystyrene nanosphere fusion

The nanosphere fusion on the mask is normally achieved by heating the substrate. When temperature reaches a certain value, the spherical nanospheres will deform and become ellipsoidal as the heating time increases. The deformed nanospheres start to contact with each other and the space between the different nanospheres becomes smaller as shown in Figure 2.9. The overheated mask is shown in Figure 2.9 (d) and the nanospheres were totally fused together. The nanosphere fusion technique is commonly applied for the fabrication of very tiny nanodot, nanopillar or nanowire arrays. Such structures are rarely employed as LTS in PV cells due to the poor light scattering capability for its small dimension. Thus, no further study was done to figure out the relation between the heating parameters and the achieved structures.
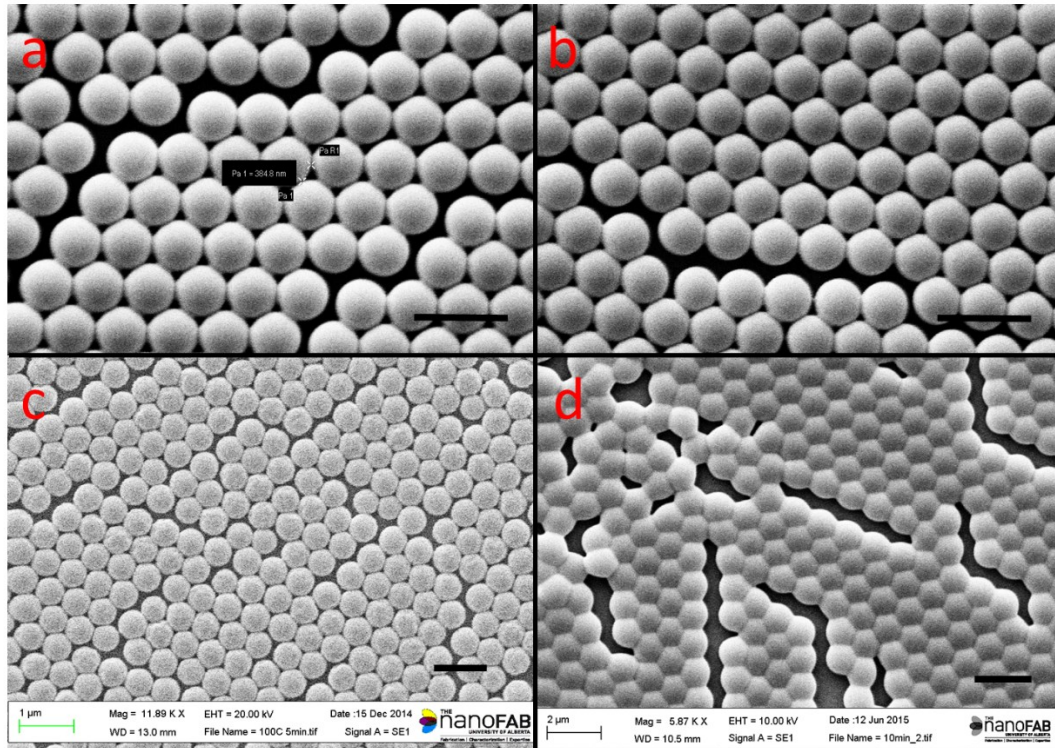
Figure 2.9 The SEM of the heated nanosphere mask under (a) 125℃ for 1min, (b) 125℃ for 2min, (c) 125℃ for 5min, (d) 125℃ for 10min. Scale bar is 1 um

2.3.3 Material deposition

The deposition process of the NSL is similar to the other lithography techniques and the electron beam physical vapor deposition (EBPVD) is utilized to deposit the metallic and dielectric material. As the target material is bombarded with the electron beam inside the deposition chamber, the atoms of the target material are less scattered and keep good deposition directionality from the cresol filled with ingot to the targeting substrate. Thus, the shape of the mask can be better preserved compared with the deposition method such as sputtering deposition. The experiment facility for EBPVD is shown in Figure 2.10. The deposition parameters for different materials used in the experiment are shown in Table 2.1. 10 nm chromium (Cr) was always deposited as adhesion layer between the glass or Si substrate and the metallic material.

Table 2.1 The deposition parameters for different material used in EBPVD

Material	Deposition rate A/s	Layer thickness
Ag	2	200 nm
Al	0.8	10 nm
SiO_2	1	200 nm
Cr	1	10 nm

Figure 2.10 The EBPVD system used for material deposition in the experiment.

2.3.4 Nanosphere removal

The removal of the nanospheres on the substrate is done with the assistant of the ultrasonic cleaner. When the material was directly deposited on the substrate covered by the mask, the nanocavity arrays were formed, filled with polystyrene nanospheres. To remove the nanospheres, the substrates were cleaned with ultrasonic in toluene, acetone and water for 10 min separately, step by step. The SEM pictures of the washed substrate for different nanosphere size are shown in Figure 2.11.
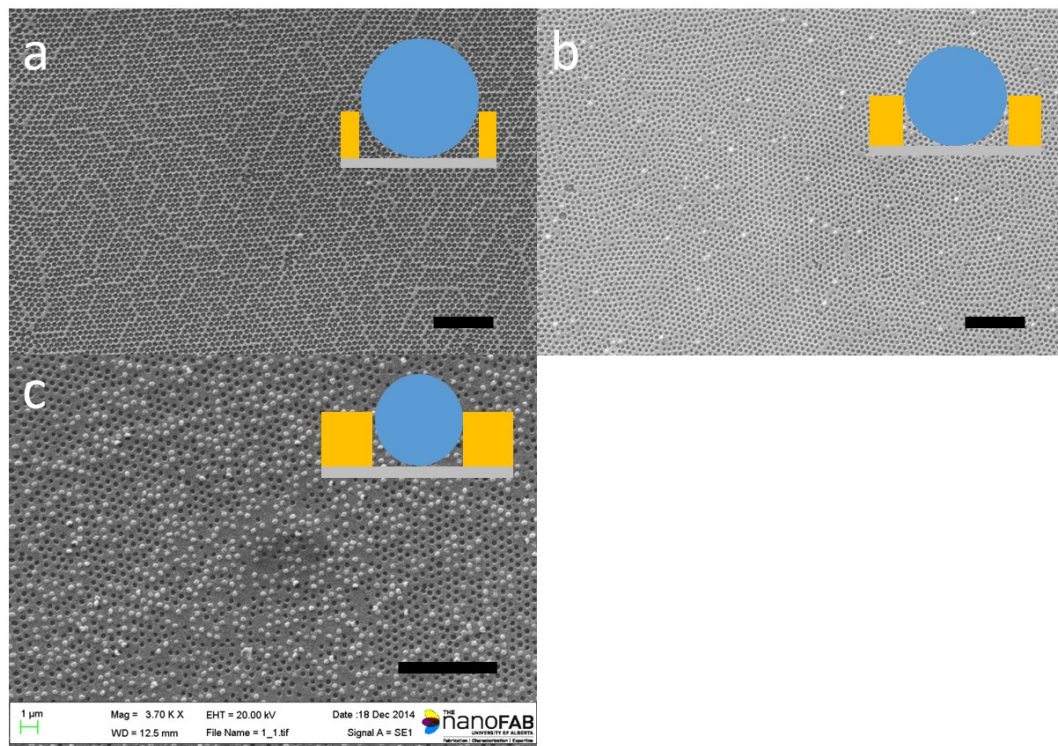
Figure 2.11 The one time washed Si substrate deposited with 200 nm Ag layer. (a) nanosphere diameter 420 nm, (b) nanosphere diameter 350 nm, (c) nanosphere diameter 300 nm. The nanospheres are totally removed for 420 nm diameter and only about 50 % of the nanospheres are removed for 300 nm diameter. The insertions demonstrate the relative position of the nanosphere (blue), the deposited structure (gold) and the substrate (grey). Scale bar is 5 um.

The substrates fabricated with larger nanosphere size are totally cleaned through one time wash. When the nanosphere size is too small, the nanosphere will be covered

by the surrounding deposited material, making it very hard to be totally removed. It is shown that about 50% of the 300 nm nanospheres cannot be removed when 200 nm Ag layer deposited. The residual nanospheres on the fabricated structure can be further cleaned by extending the ultrasonication time and repeatable washes.

2.4   Summary

The experiment condition for the NSL with the 500 nm polystyrene nanosphere has been carefully optimized to get the crystalline nanosphere mask. High quality mask has been obtained using the self-assembly of nanospheres at the water-air interface. The mask was successfully transferred from the water surface to both hydrophilic and hydrophobic substrates with the assistance of the oxygen plasma hydrophilic treatment. Additionally, the mask modification and the nanosphere removal process have been repeatedly performed to get most stable and reliable parameter for the following experiment. In the following chapters, the NSL is applied for the purpose of fabricating large area and high quality metallic and dielectric 2D LTS to help increasing the performance of PV devices.

Reference

1.   Dill, F.H., *Optical lithography.* IEEE Transactions on Electron Devices, 1975. **22**(7): p. 440-444.

2.   Rothschild, M., et al., *Lithography at a wavelength of 193 nm.* IBM Journal of Research and Development, 1997. **41**(1.2): p. 49-55.

3.   Chou, S.Y., P.R. Krauss, and P.J. Renstrom, *Nanoimprint lithography.* Journal of Vacuum Science & Technology B, 1996. **14**(6): p. 4129-4133.

4.   Pease, R.F.W., *Electron beam lithography.* Contemporary Physics, 1981. **22**(3): p. 265-290.

5.   Melngailis, J., *Focused ion beam lithography.* Nuclear Instruments and Methods in Physics Research Section B: Beam Interactions with Materials and Atoms, 1993. **80**: p. 1271-1280.

6.   Gates, B.D., et al., *New Approaches to Nanofabrication: Molding, Printing, and Other Techniques.* Chemical Reviews, 2005. **105**(4): p. 1171-1196.

7.   Hennessy, K., et al., *Square-lattice photonic crystal microcavities for coupling to single InAs quantum dots.* Applied Physics Letters, 2003. **83**(18): p. 3650-3652.

8.   Zhu, X., et al., *Ultrafine and Smooth Full Metal Nanostructures for Plasmonics.* Advanced Materials, 2010. **22**(39): p. 4345-4349.

9.   Hulteen, J.C. and R.P. Van Duyne, *Nanosphere lithography: A materials general fabrication process for periodic particle array surfaces.* Journal of Vacuum Science & Technology A, 1995. **13**(3): p. 1553-1558.

10.   Kosiorek, A., et al., *Shadow Nanosphere Lithography: Simulation and Experiment.* Nano Letters, 2004. **4**(7): p. 1359-1363.

11.   Li, H., et al., *Large-Area Well-Ordered Nanodot Array Pattern Fabricated With Self-Assembled Nanosphere Template.* IEEE Sensors Journal, 2008. **8**(6): p. 880-884.

12.   Haynes, C.L., et al., *Angle-Resolved Nanosphere Lithography: Manipulation of Nanoparticle Size, Shape, and Interparticle Spacing.* The Journal of Physical Chemistry B, 2002. **106**(8): p. 1898-1902.

13.   Fischer, U.C. and H.P. Zingsheim, *Submicroscopic pattern replication with visible light.* Journal of Vacuum Science & Technology, 1981. **19**(4): p. 881-885.

14.   Schäfer, C.G., et al., *Fully Reversible Shape Transition of Soft Spheres in Elastomeric Polymer Opal Films.* Langmuir, 2013. **29**(36): p. 11275-11283.

15.   Shiu, J.-Y., et al., *Fabrication of Tunable Superhydrophobic Surfaces by Nanosphere Lithography.* Chemistry of Materials, 2004. **16**(4): p. 561-564.

16.   Kosiorek, A., et al., *Fabrication of Nanoscale Rings, Dots, and Rods by Combining Shadow Nanosphere Lithography and Annealed Polystyrene Nanosphere Masks.* Small, 2005. **1**(4): p. 439-444.

17.   Haes, A.J., et al., *Solution-Phase, Triangular Ag Nanotriangles Fabricated by Nanosphere Lithography.* The Journal of Physical Chemistry B, 2005. **109**(22): p. 11158-11162.

18.   Hulteen, J.C., et al., *Nanosphere Lithography: Size-Tunable Silver Nanoparticle and Surface Cluster Arrays.* The Journal of Physical Chemistry B, 1999. **103**(19): p. 3854-3863.

19.   Hering, K., et al., *SERS: a versatile tool in chemical and biochemical diagnostics.* Analytical and Bioanalytical Chemistry, 2008. **390**(1): p. 113-124.

20.   Schmidt, J.P., S.E. Cross, and S.K. Buratto, *Surface-enhanced Raman scattering from ordered Ag nanocluster arrays.* The Journal of Chemical Physics, 2004. **121**(21): p. 10657-10659.

21.   Debnath, R., et al., *Ambient-Processed Colloidal Quantum Dot Solar Cells via Individual Pre-Encapsulation of Nanoparticles.* Journal of the American Chemical Society, 2010. **132**(17): p. 5952-5953.

22.   Jensen, T.R., et al., *Nanosphere Lithography: Effect of the External Dielectric Medium on the Surface Plasmon Resonance Spectrum of a Periodic Array of Silver Nanoparticles.* The Journal of Physical Chemistry B, 1999. **103**(45): p. 9846-9853.

23.   Cheung, C.L., et al., *Fabrication of nanopillars by nanosphere lithography.* Nanotechnology, 2006. **17**(5): p. 1339.

24.   Yu, J., et al., *Preparation of High-Quality Colloidal Mask for Nanosphere Lithography by a Combination of Air/Water Interface Self-Assembly and Solvent Vapor Annealing.* Langmuir, 2012. **28**(34): p. 12681-12689.

25.   Chen, W., R.H.W. Lam, and J. Fu, *Photolithographic surface micromachining of polydimethylsiloxane (PDMS).* Lab on a chip, 2012. **12**(2): p. 391-395.

26.   Hall, A.S., S.A. Friesen, and T.E. Mallouk, *Wafer-Scale Fabrication of Plasmonic Crystals from Patterned Silicon Templates Prepared by Nanosphere Lithography.* Nano Letters, 2013. **13**(6): p. 2623-2627.

Chapter 3. Observation of localized surface plasmons and hybridized surface plasmon polaritons on 2D Ag grating

The metallic grating is an important category of LTS due to its high light scattering efficiency, which is introduced by the SP excitation. The SP can be used for light confinement at the metal-dielectric interface and the caused light concentration effect can help to increase the unit volume absorption in thin film materials. Thus, the study of SP excitation on the metallic grating surface is of great interest for the research of the light trapping by metallic gratings.

3.1 Introduction

SP has long been an area of interest since its prediction by Ritchie in 1950s.[1] This area draws large attentions in last two decades for the discovery of extraordinary optical transmission (EOT),[2] in which surface plasmon polariton (SPP) was proposed to describe the unique coupling of light with metal surface. In recent years, SPP has shown applications in various fields, such as nano-scale plasmon waveguide,[3] SERS,[4] and thin film solar energy harvesting.[5, 6] SPP is generated by the coupling of incident EM wave with free electrons in metal to convert the EM wave in to a bound wave, which propagates along the metal-dielectric interface. However, the wave vector of the bound wave is proved to be slightly larger than that in free space based on rigorous derivation from Maxwell equations. To overcome this mismatch of wave vectors, additional wave vector is appended to the incoming EM wave using gratings or optical prisms. Compared with one-dimensional (1D) metallic gratings, two-dimensional (2D) metallic gratings can excite SPP regardless of the

polarization of incident light.[7]

Previous demonstrations[8] of fabricating 2D metallic gratings by electron beam lithography are costly and time consuming. Thus, it is urgent to develop a more efficient and convenient method to fabricate large-area metallic gratings for upcoming SPP applications. Mallouk[9] has recently proposed a method to prepare large-scale patterned silicon template for 2D grating fabrication with NSL and this approach is proven to be reliable for large-scale SPP grating fabrication. The fabricated large-area 2D grating is essential in the applications requiring large sample area and comparatively lower lattice quality, such as patterned reflection electrodes of solar cells and SERS devices. In addition to SPP, LSP is caused by the collective resonance of electrons in the metal particles under external driven EM field. As for the LSP on metallic gratings, it is unlikely to obtain accurate analytical solutions due to the large dimension. Though LSP on metallic gratings is unpredictable with conventional numerical calculation, the existence of LSP can still be confirmed with FDTD simulation and experimental results based on unique LSP properties such as large near-field enhancement and weak dependence on excitation condition.

In this chapter, the basic concept of the SP including LSP and SPP are introduced. In the experimental part, we fabricated large-area silver (Ag) gratings with the assistant of NSL. The SP excitation and surface mode hybridization was confirmed based on the reflection and absorption spectra of the fabricated 2D grating. Additionally, the electrical field profile near the grating surface with the excitation of the SPP was simulated with the FDTD method. As a reference, the 2D silicon dioxide (SiO_2) dielectric grating on silver film was also fabricated, and it is shown that the LSP only exists on metallic gratings.

3.2   Mechanism of the SP and its experimental measurement

3.2.1 Localized surface plasmon

LSP refers to the SP excited on the metallic particle with small dimension, normally at the nanoscale.[10, 11] The metallic particles can be considered as isolated islands with a lot of free electrons and the range of the electrons' movement are all confined within the boundary. With the external driven EM field, the electrons inside the metallic particle will oscillate under the electric static force. As is known, there is a resonant frequency for the metallic material according to the Drude model, in which the electrons are regarded as classical particles moving in space, and the electron oscillation becomes most intense when the frequency of driving EM wave is closer to the resonant frequency. In this model, the free resonant frequency is merely determined by the property of the metallic material. However, when it comes to nanoscale metallic structures, the resonant frequency is referred to as LSP frequency and it is observed that the LSP frequency depends not only on material, but also on the particle shape. Under the resonant frequency, the electron oscillation can generate EM field like a dipole and change the EM field distribution in surrounding space. There are two figures of merit in the study of LSP on metal particles: the resonant frequency of LSP and the intensity of generated EM field. For the simplest structure of nanosphere, analytical solution can be obtained by the Mie theory. It is discovered that the LSP resonant frequency of the metallic sphere is related to the radius of the sphere, as well as the EM field distribution. The EM field intensity generated near the metal sphere surface could be hundreds of times larger than the external driven EM field.[11] With the growing interest of LSP in recent years, more advanced numerical analysis methods have been demonstrated to analyze the LSP of nanoparticles with more complicated structure, such as nanorod,

nanotriangle and nanoshell etc.[12-14]

3.2.2 Surface plasmon polariton

SPP is another kind of light-metal interaction different from LSP in the way that how electrons behave under external EM field. As we have mentioned, the electrons excited by LSP are confined inside the metallic nanoparticle, which is considered as a localized space. However, in case of SPP, the movement of electrons is along the metal-dielectric interface which is a two dimensional plane. The electrons form a surface wave with periodic distributed positive and negative net charges locally and change the EM field intensity near the interface.[11] The SPP frequency is determined mainly by the property of the metallic and dielectric materials that form the interface and depends less on the surface roughness and shape. With the excitation of the SPP, the energy of the incident driven EM field can be converted to the energy of the bounding SPP surface wave and increase the EM field intensity near the metallic surface.

As the SPP exists on the panel structures, the electrodes of the PV cells have inherent advantage to be designed for SPP excitation to improve the device performance.[5, 15] Despite the flat panel, the excitation of the SPP requires the match of excitation EM field wave vector with the SPP wave vector, where special techniques should be applied.[11] One common practice is by adding the periodic gratings on the metallic panel, which has been demonstrated in many research works. This method was employed to generate SPP in our study. The detailed analysis of the SPP excitation observed on the 2D nanocavity Ag grating will be discussed in the subchapter 3.4.

3.2.3 Surface plasmon hybridization and experiment measurement

In recent years, the coupling of SPP and LSP has been studied on the metal-insulator-metal (MIM) gratings,[16] in which the metal island on the top of insulation layer can excite LSP and the bottom metal layer can support SPP. The coupling of LSP and SPP becomes stronger as the resonant peak of SPP and LSP approaches. In a recent report,[17] the coupling of SPP and LSP still exists even if the insulation layer between metals was completely removed and it leads to hybridized SPP modes on the grating interface. However, only forward propagating SPP was observed using the Kretschmann coupling geometry.

In our experiments, we excited LSP and SPP on the self-assembled 2D nanocavities using a broad band light source with the monochromator. We continuously changed incident angles on the grating, and detected both specular and diffuse reflected light as shown in the schematic in Figure 3.1. Two kinds of samples, the metallic grating and the dielectric grating, with the same geometry were tested in the experiment. Perkin-Elmer lambda 1050 spectrophotometer was employed to measure sample reflection and a 6 inch integration sphere was used for light collection to eliminate the influence of grating diffraction. The incident light was non-polarized and the polarization is proven to have no influence on the SP excitation on systematic 2D grating according to a recent study.[7] All samples were exposed to air during the measurement. We observed both forward and backward propagating SPPs using the grating coupling geometry, and the LSP and SPP hybridization phenomenon was observed. By analyzing resonance wavelengths of hybridized SPPs from experimental results and numerical calculations, we confirmed the conclusion from previous report[16] that the coupling of SPP and LSP becomes stronger as the resonances of SPP and LSP get closer.
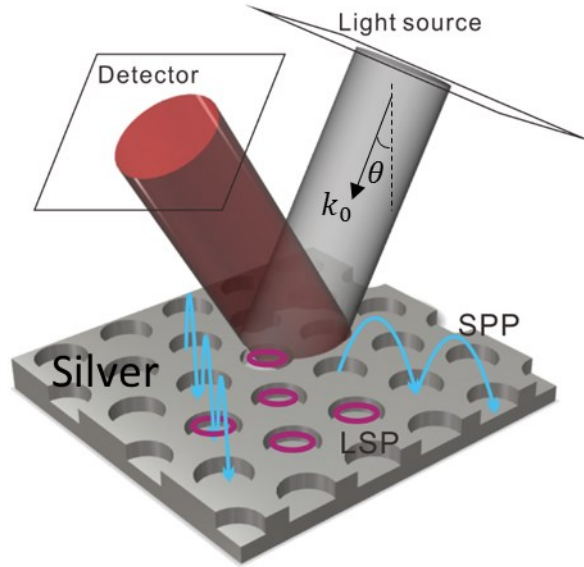
Figure 3.1 The schematic of the measurement. SPP and LSP are excited on the structure by incident light. Both specular and diffuse reflections are captured in experiment.

3.3　Sample fabrication and surface morphology

Nanospheres lithography is an efficient method to fabricate large-area periodic nanostructures.[18] Here we applied self-assembled nanosphere to fabricate periodic nanocavity patterns for metallic gratings and dielectric gratings. The process flow is shown in Figure 3.2. The 500 nm diameter polystyrene (PS) sphere was purchased from Sigma-Aldrich, and the Si wafer was used as substrate. In the fabrication of silver (Ag) 2D structure, self-assembled colloidal sphere mask was prepared with the method described in chapter 2. In order to obtain the 2D cavity structure, the size of PS sphere was reduced with oxygen plasma RIE, with 20 W chunk power, 5 sccm flow rate and 63 s dealing time. Afterward, 75 nm Ag film was deposited on sphere mask with EBPVD (deposition rate 1A/s). Then, we removed the PS nanosphere with ultrasonic cleaning for 10 min, emerging in toluene. Finally, another 200 nm Ag film was deposited with EBPVD to form the metallic grating. As for the SiO2 dielectric grating, the fabrication process was modified compared with metallic grating as also

shown in Figure 3.2. Another 10 nm aluminum (Al) layer was inserted between the SiO2 and Ag film to protect the Ag from the oxygen plasma during RIE process and the thickness of Al is optimized to cause the slightest impact to the structure. Finally, 75nm thick SiO2 was deposited on the sphere mask on the top of metal. The ultrasonic clean is used to remove the PS nanospheres from the substrate and the toluene is proven to be a good solvent for the sphere removal.
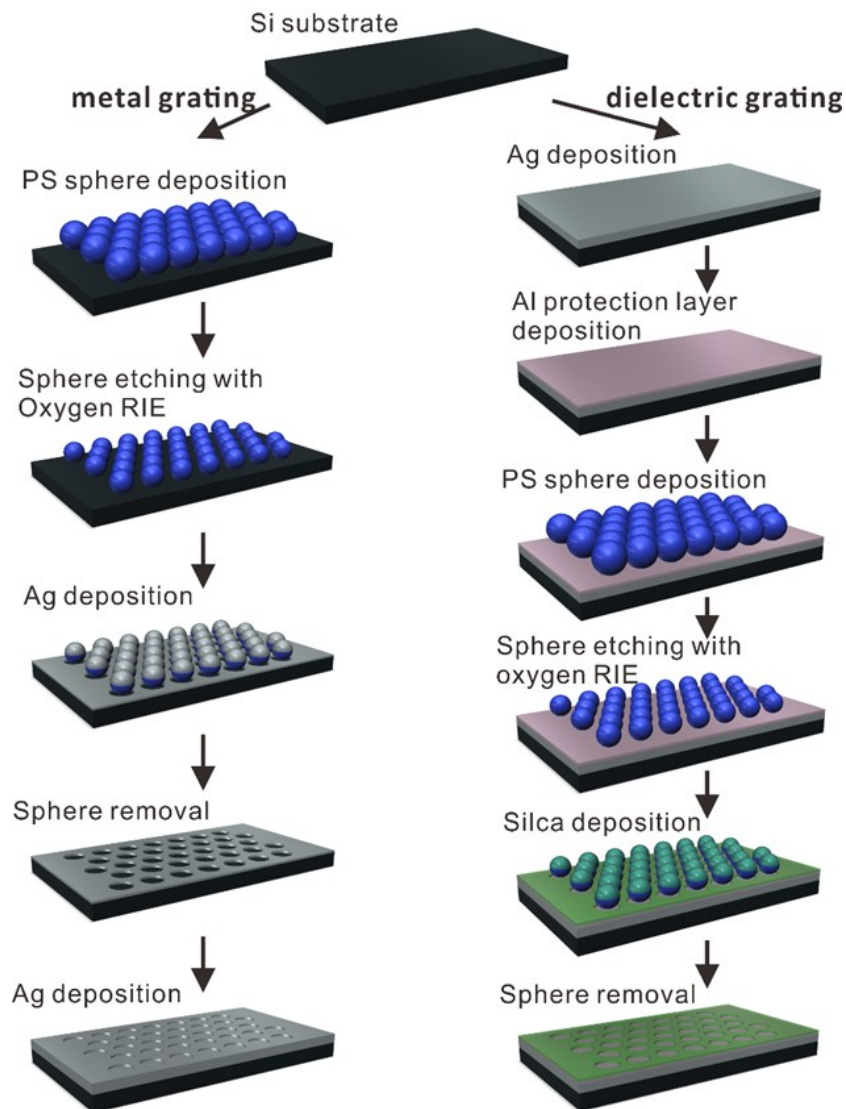
Figure 3.2 The fabrication process flow of 2D metallic grating (left) and dielectric grating (right).

The surface morphology of the fabricated samples is characterized with the SEM

and the atomic force microscope (AFM) as shown in Figure 3.3 (a). The SEM of 2D nanocavity array shows that the nanocavities strictly conform the hexagonal distribution and the size of the nanocavities are almost uniform. However, the gaps between adjacent nanocavities has slight difference. That is because the nanospheres are not closely packed and the distance between different nanospheres are changed when patterns on the PS nanosphere mask is transferred onto the targeted substrate. The issue of how to keep the distance of nanospheres unchanged is still a challenge for the NSL nowadays. The AFM picture for grating is shown in Figure 3.3 (b). The cylinder cavity is about 360 nm in diameter and 75 nm in depth.
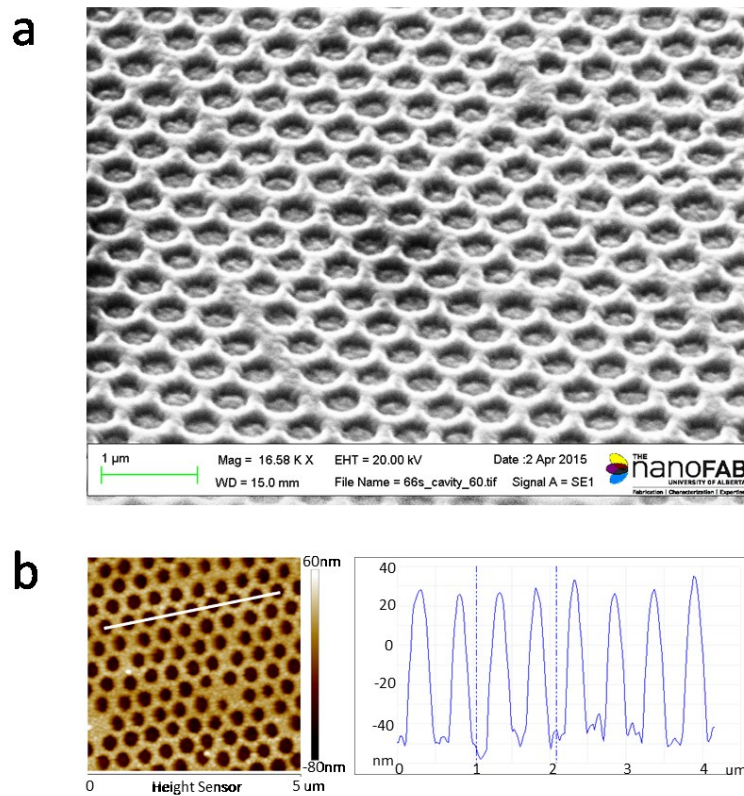
Figure 3.3 (a) The SEM showing the surface of the fabricated 2D Ag nanocavity array grating. (b) The AFM image of the grating surface. The cross section at position marked with white line is also presented, showing the detailed value of the dimension of the nanocavities.

3.4 Results analysis and discussion

The experimental results of the normalized absorption for the 2D nanocavity Ag grating is shown in Figure 3.4, in which the intrinsic absorption of Ag is eliminated by subtracting the results with flat Ag film absorption. As shown, red color regions indicate the wavelength with strong absorption on the grating under specific incident angle. The strong absorption around 395 nm was independent of the incident angle, representing the existence of LSP. The two incident angle dependent absorption lines were attributed to SPPs bound to the grating surface. We used the following theory to explain our observations.

On the metal-dielectric interface, the propagation constant of SPP can be expressed as:

$$\beta = k_0 \sqrt{\frac{\varepsilon_d \varepsilon_m}{\varepsilon_d + \varepsilon_m}} \tag{3.1}$$

where β is the SPP propagation constant on the flat metal surface, k_0 is the wavenumber of incident light in free space, ε_d and ε_m are the permittivity of dielectric and metallic materials, respectively. For 1D grating, SPP can propagate along the direction of the projection of incident light on the interface, or along the opposite direction. Thus, in the grating coupling geometry, the coupling is:

$$\pm\beta = k_0 sin\theta \pm mk_B, \text{ m=1, 2, 3……} \tag{3.2}$$

where k_B is the wavenumber of the 1D grating and θ is the incident angle. Here $k_B = 2\pi/\Lambda$, and Λ is the grating constant. Combining equation (3.1) and equation (3.2), we derived the following expression for forward and backward propagating SPP.

Forward propagating SPP:

$$k_0 \operatorname{Re}(\sqrt{\frac{\varepsilon_d \varepsilon_m}{\varepsilon_d + \varepsilon_m}}) = k_0 \sin\theta + mk_B \text{ , m=1, 2, 3……} \tag{3.3}$$

Backward propagating SPP:

$$-k_0 \, \mathrm{Re}(\sqrt{\frac{\varepsilon_d \varepsilon_m}{\varepsilon_d + \varepsilon_m}}) = k_0 \sin\theta - mk_B \quad , \text{m=1, 2, 3……} \qquad (3.4)$$

It is well known that the first order diffraction pattern of hexagonal gratings consists of 6 distinct directions. This is due to the fact that any general hexagonal diffraction grating can be decomposed into three identical two-dimensional diffraction gratings[19] with different orientations. Thus, each grating contributes to 2 diffraction directions in the first order diffraction pattern, and the grating constant should be revised to $\Lambda = \sqrt{3}a/2$, where a is the distance between adjacent holes. In our experiments, a equals to 500 nm.
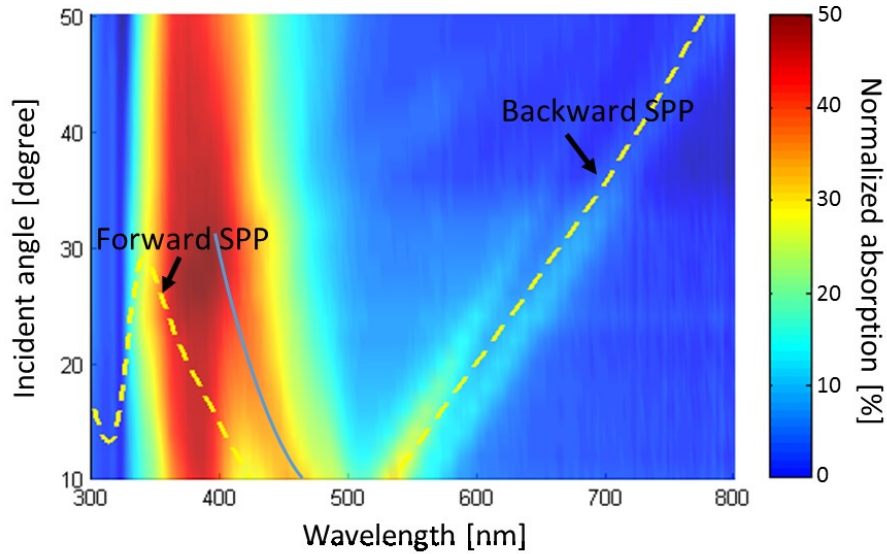
Figure 3.4 The measured normalized absorption of the silver grating as a function of incident angle and wavelength. The blue solid line is a guide to the eye for the forward SPP observed in experiment. The yellow dash lines are the calculated resonant wavelengths of forward and backward propagating SPPs as a function of different incident angle.

Here we apply the same concept, and only consider SPP excited from one of the three gratings. Using the dielectric constant of air and ε_m of Ag from Johnson and Christy,[20] we calculated the SPP modes and found that only the first order (m=1) forward and backward propagating SPP modes and the second order (m=2) backward

propagating SPP mode are in the observation wavelength range. However, we only observed the first order SPP modes that are excited and propagated along grating surfaces in experiments. Thus, we plotted calculated first order SPP modes in Figure 3.4. For the backward propagating SPP, the calculated values match with the observed wavelengths in experiment results. For the forward propagating SPP, there is about 40 nm difference in wavelength between calculation and experimental results. As SPPs were hybridized modes arising from the coupling between SPP and LSP,[17] we conclude that the coupling of SPP and LSP becomes stronger as the resonances of SPP and LSP get closer.

3.5   Numerical simulation of 2D gratings

To get a further understanding of LSP and SPP modes observed, we have studied the near-field profile of the different modes observed with FDTD simulation. A hexagonal Ag grating with the 380 nm diameter, 75 nm depth and 500 nm spacing nanocavity is designed. The plane wave polarizing in the incident plane is utilized as the light source and 10 degree incident angle is introduced. The incident plane overlaps with one of the symmetric plane of the 2D array. Bloch and perfect matched layer (PML), which can be considered as total absorber, boundary conditions are used in the grating parallel and normal directions, respectively. Environment index is set to 1 and the refractive index from Johnson and Christy[20] is applied to Ag. Figure 3.5 (a) shows the normalized near-field profile at wavelength 395 nm. It is shown that the field enhancement occurs inside the metal cavity extending from the wall to the bottom of cavity and the hot spot of electric field appears at the bottom corners of the cavity. According to the normalized electric field profile, E-field above the cavity is around 1 and barely gets affected, suggesting that the mode is a LSP mode of the metal nanocavity. As a comparison, The E-field profile at the wavelength of 465 nm for SPP is shown in Figure 3.5 (b). The SPP affects the electric field to a

wider range and the E-field at 200 nm above the grating interface is still influenced. Figure 3.5 (c) compares the E-field enhancement at 10 nm from the grating surface caused by LSP and SPP. It is clearly seen that LSP provides 10 times enhancement in E-field intensity at certain locations, and SPP can achieve better enhancement across the whole surface. The full reflection spectra of 2D Ag grating at 10 degree incidence are shown in Figure 3.6 (a). The absorption peak of the reference (flat surface) is due to the intrinsic absorption of Ag. Peak a, peak b, and peak c correspond to the LSP, backward and forward propagating SPPs, respectively. The position of all peaks match well with the simulation, indicated as peak a', peak b', peak c'.
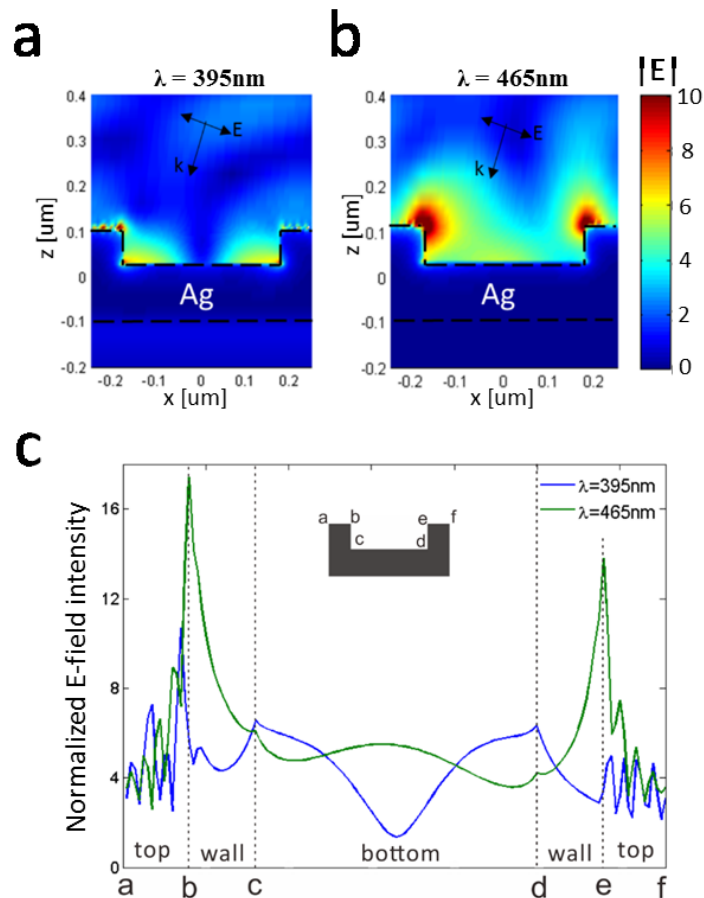
Figure 3.5 The normalized E-field profile near the metallic grating at the wavelength of 395 nm (a) and 465 nm (b) at 10 degree incidence. (c) E-field intensity at 10 nm away from the grating surface. The a, b, c, d, e, f indicate different position on the grating as shown in the insertion.

We also carried out a sanity check using dielectric gratings with the same 2D geometry of nanocavity array. The dielectric grating consists of periodic SiO_2 nanostrcutures on thick Ag films. As the nanocavity is made of SiO_2, no electron resonance would exist, thus no LSP mode can be supported. For the simulation of dielectric grating, a thin layer of 4 nm Al is insert between the SiO_2 structure and the Ag film. Here a thinner layer of Al is used for the fact that Al is partially oxidized during oxygen plasma RIE. The measured reflection of the dielectric grating is shown in the Figure 3.6 (b). Both forward and backward propagating SPPs are observed in simulation and only forward propagating SPP is observed in experiment. Besides, the LSP disappears for dielectric grating according to both simulation and experimental results.
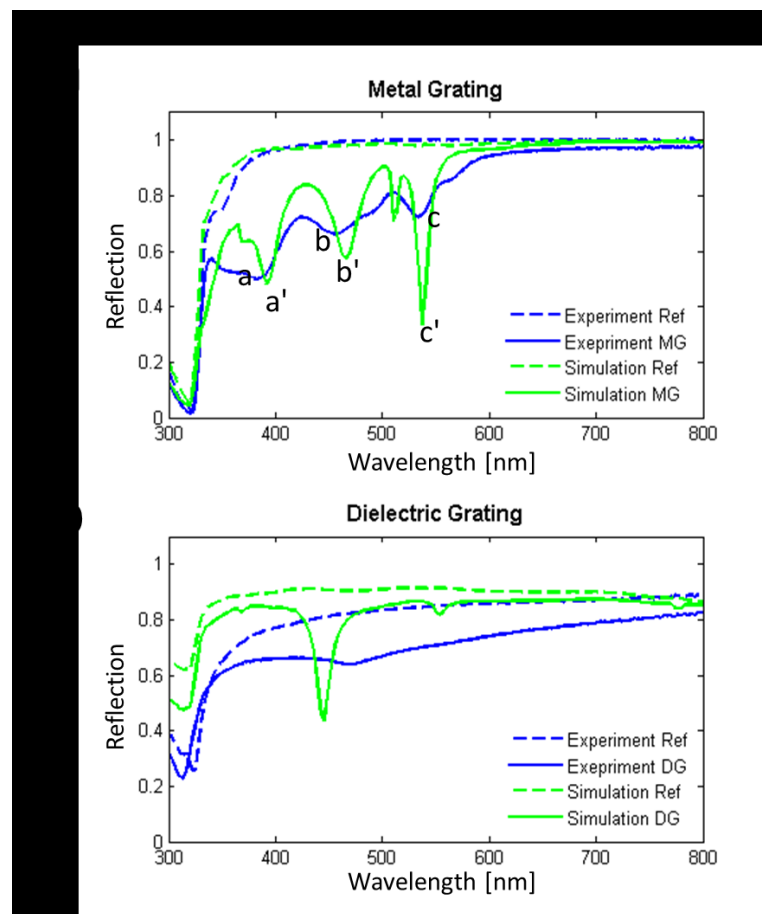
Figure 3.6 The experiment and simulation result of reflection spectra for (a) metallic grating (MG) and (b) dielectric grating (DG) with 10 degree incident angle.

3.6　Summary

In summary, we have fabricated large-scale 2D periodic nanocavity array employing self-assembled nanospheres. We performed both theoretical and experimental studies of SPP and LSP resonances excited on these nanostructures. We observed two SPP modes and one LSP mode, and one of SPP modes was attributed to strong hybridization between SPP and LSP. The E-field enhancement for LSP and SPP were studies with FDTD simulation and the existence of LSP mode was further justified with additional dielectric grating. The cheap and efficient way to fabricate 2D metal grating with large near-field enhancement is of great importance for the application in thin film PV cells to increase the device performance.

Reference

1.   Ritchie, R.H., *Plasma Losses by Fast Electrons in Thin Films.* Physical Review, 1957. **106**(5): p. 874-881.

2.   Ebbesen, T.W., et al., *Extraordinary optical transmission through sub-wavelength hole arrays.* Nature, 1998. **391**(6668): p. 667-669.

3.   Tanaka, K. and M. Tanaka, *Simulations of nanometric optical circuits based on surface plasmon polariton gap waveguide.* Applied Physics Letters, 2003. **82**(8): p. 1158-1160.

4.   Anker, J.N., et al., *Biosensing with plasmonic nanosensors.* Nat Mater, 2008. **7**(6): p. 442-453.

5.   Atwater, H.A. and A. Polman, *Plasmonics for improved photovoltaic devices.* Nat Mater, 2010. **9**(3): p. 205-213.

6.   Yang, J., et al., *Plasmonic Polymer Tandem Solar Cell.* ACS Nano, 2011. **5**(8): p. 6210-6217.

7.   Aydin, K., et al., *Broadband polarization-independent resonant light absorption using ultrathin plasmonic super absorbers.* Nat Commun, 2011. **2**: p. 517.

8.   Chu, Y., M.G. Banaee, and K.B. Crozier, *Double-Resonance Plasmon Substrates for Surface-Enhanced Raman Scattering with Enhancement at Excitation and Stokes Frequencies.* ACS Nano, 2010. **4**(5): p. 2804-2810.

9.   Hall, A.S., S.A. Friesen, and T.E. Mallouk, *Wafer-Scale Fabrication of Plasmonic Crystals from Patterned Silicon Templates Prepared by Nanosphere Lithography.* Nano Letters, 2013. **13**(6): p. 2623-2627.

10.   Myroshnychenko, V., et al., *Modelling the optical response of gold nanoparticles.* Chemical Society Reviews, 2008. **37**(9): p. 1792-1805.

11.   Maier, S.A., *Plasmonics: Fundamentals and Applications*. 2010: Springer US.

12.   Félidj, N., et al., *Multipolar surface plasmon peaks on gold nanotriangles.* The Journal of Chemical Physics, 2008. **128**(9): p. 094702.

13.   Höflich, K., U. Gösele, and S. Christiansen, *Near-field investigations of nanoshell cylinder dimers.* The Journal of Chemical Physics, 2009. **131**(16): p. 164704.

14.   Nishijima, Y., et al., *Plasmon-Assisted Photocurrent Generation from Visible to Near-Infrared Wavelength Using a Au-Nanorods/TiO2 Electrode.* The Journal of Physical Chemistry Letters, 2010. **1**(13): p. 2031-2036.

15.   Ferry, V.E., et al., *Optimized Spatial Correlations for Broadband Light Trapping Nanopatterns in High Efficiency Ultrathin Film a-Si:H Solar Cells.* Nano Letters, 2011. **11**(10): p. 4239-4245.

16.   Chu, Y. and K.B. Crozier, *Experimental study of the interaction between localized and propagating surface plasmons.* Optics Letters, 2009. **34**(3): p. 244-246.

17.   Sarkar, M., et al., *Hybrid Plasmonic Mode by Resonant Coupling of Localized Plasmons to Propagating Plasmons in a Kretschmann Configuration.* ACS Photonics, 2015. **2**(2): p. 237-245.

18.   Peng, K., et al., *Ordered silicon nanowire arrays via nanosphere lithography and metal-induced etching.* Applied Physics Letters, 2007. **90**(16): p. 163123.

19.   Iwata, K., et al., *Three-dimensional profiling using the Fourier transform method with a hexagonal grating projection.* Applied Optics, 2008. **47**(12): p. 2103-2108.

20.   Johnson, P.B. and R.W. Christy, *Optical Constants of the Noble Metals.* Physical Review B, 1972. **6**(12): p. 4370-4379.

Chapter 4. Study of complementary nanostructure for light trapping in PbS CQD solar cells

The large area patterned electrode is the most important part to achieve light trapping in PV devices. In this chapter, a fabrication process for large area ITO electrode with nanocavity and nanopillar array is proposed. The PbS CQD solar cell integrated with nanocavity and nanopillar arrays are investigated through numerical analysis. Large absorption enhancement is observed at the resonant wavelength for both nanocavity and nanopillar arrays, showing the great potential for the application of nanostructures in solar energy harvesting.

4.1 Introduction

In the last few years, colloidal quantum dot (CQD) solar cells have received a great deal of attention due to their potential for large-area, high-throughput, and low-cost manufacturing.[1] Despite all the achievements in CQD synthesis, surface treatment and film deposition technologies,[2] the power conversion efficiency of this type of solar cell continues to lag behind traditional silicon solar cells. Because of the lack of long diffusion lengths for photo-generated carriers in CQD films, a CQD film capable of taking advantage of all the incident solar power would be too thick to extract all the generated carriers, leading to an absorption-extraction trade-off.[3-5] Light trapping, or effectively increasing optical path lengths in the absorbing material through structuring without any change in light absorbing material's thickness, is one option to overcome the trade-off.[6]

Periodic nanostructured gratings have been extensively explored for light

trapping in various types of thin-film solar cells and various silicon or metamaterial-based structures have been proposed, such as nanopillar, nanowire, nanocavity, pyramid arrays.[7-9] The downside, however, is that these structures are difficult to fabricate due to their complicated structures or material compositions. Metallic gratings have also been considered for light harvesting enhancement by taking advantage of SP.[10-12] However, parasitic light absorption by metallic structures, which can compete against useful absorption in light absorbing layer, has severely limited the application of metallic nanostructures in photovoltaic devices.[13]

Recently, it was reported that periodic nano-branch ITO electrodes as diffraction gratings can be used for light absorption enhancement in CQD solar cells.[14] Using numerical simulations, a significant polarization-independent broadband light absorption enhancement was observed for two-dimensional ITO nano-branch gratings and the absorption enhancement was demonstrated to be almost independent of common fabrication flaws in nano-branch structure. On the other hand, current fabrication technologies are unable to implement the fabrication of such nanostructures due to the difficulty of keeping the periodicity of the structure over a large area and incorporating CQDs into such porous structure.

In order to apply a periodic nanostructure for practical light trapping in solar cells, maintaining the periodicity of the structure over a large area is the key requirement. Therefore, the fabrication process used to impose the periodic pattern must be able to produce periodic patterns over large areas in an inexpensive way. Recent advances in large-scale nanofabrication techniques have allowed sophisticated nanostructures to be employed in solar cells and photodetectors with impressive results.[15, 16] In this chapter, we proposed two experimentally available nanostructures (nanocavity and nanopillar) for light absorption enhancement in CQD solar cells due to their potential for easy large-area fabrication and CQD film incorporation. The numerical simulation has been conducted to investigate the

absorption enhancement in the PbS PV device with the incorporation of structures.

4.2   Structure fabrication and device design

4.2.1 The fabrication of complementary nanocavity and nanopillar array

The nanopillar and nanocavity structures were fabricated for the demonstration of LST in PbS CQD solar cell since their large area pattern can be easily fabricated with the mentioned NSL process in chapter 2. As a proof of concept, PDMS nanopillar and nanocavity arrays were fabricated utilizing NSL. The proposed process steps for fabrication of nanocavity and nanopillar arrays is presented schematically in Figure 4.1. Firstly, colloidal nanosphere mask was self-assembled at water surface and then deposited on a Si substrate. After nanosphere mask formation, oxygen plasma was employed to shrink the nanospheres to ideal diameter needed for the desired structure through RIE with 300 W source power, 20 W chunk power and 5 sccm oxygen flow rate for 1 min. The next step was to deposit the desired material, in this case Ag, on the sample covered by the mask. 80 nm Ag was deposited with 2 Å/s deposition rate. The final step was to remove the nanospheres on the mask with ultrasonic cleaning in acetone and toluene, after which the nanocavity array was formed on the substrate. Another 200 nm Ag is deposited with EBPVD to form a completed Ag nanocavity array. In addition to being a standalone light trapping structure, the fabricated nanocavity array on Si substrate can be utilized as mold for fabrication of nanopillar array through PDMS casting and peeling off. Because the nanocavity array can act as a mold to form nanopillar array.

PDMS material was prepared by mixing silicone elastomer with curing agent from a Sylgard 184 kit (Dow Corning) in 10 wt% ratio. The mixture was then degassed in a desiccator for 30 min. To form the patterns on the PDMS, the prepared

mixture was then poured onto fabricated Ag nanocavity mold placed in the petri dish. This PDMS pouring process should be conducted in vacuum to avoid the generation of bubbles between mold and PDMS. Afterward, The PDMS inside the petri dish was cured on a hot plate of 80℃ for 2h, after which it was peeled off from the Ag nanocavity mold.
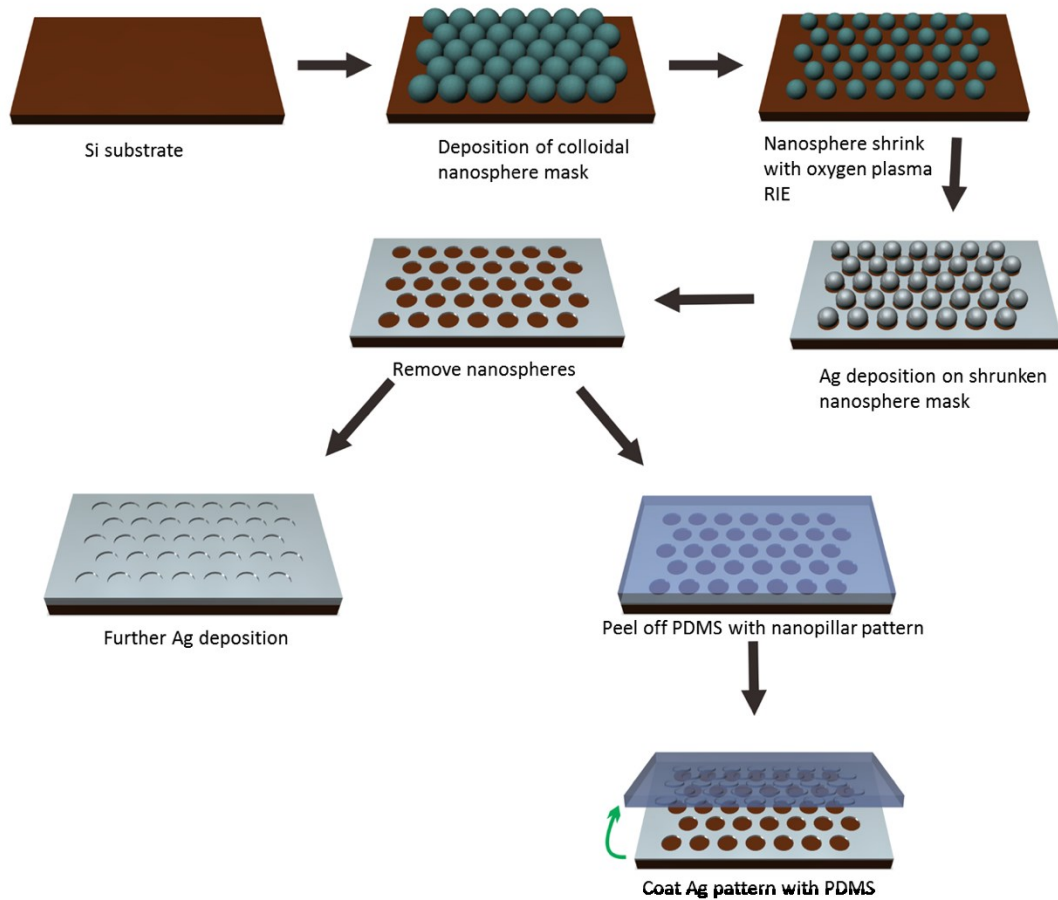
Figure 4.1 The proposed process flow for fabrication of nanocavity and nanopillar arrays. The fabrication of Ag nanocavity array and the PDMS nanopillar array are shown respectively.

The SEM images of the cavity and pillar arrays fabricated using the described fabrication process are shown in Figure 4.2 (a) and 4.2 (b). We believe a similar procedure with minimal modification can be used to fabricate well-defined ITO nanocavity and nanopillar arrays for conductive electrodes of solar cells. Substituting the silver with ITO in material deposition step will easily lead to ITO nanocavity

58

structure and depositing ITO on top of fabricated PDMS nanopillars can form the desired ITO nanopillars suitable for light absorption enhancement in CQD solar cells.
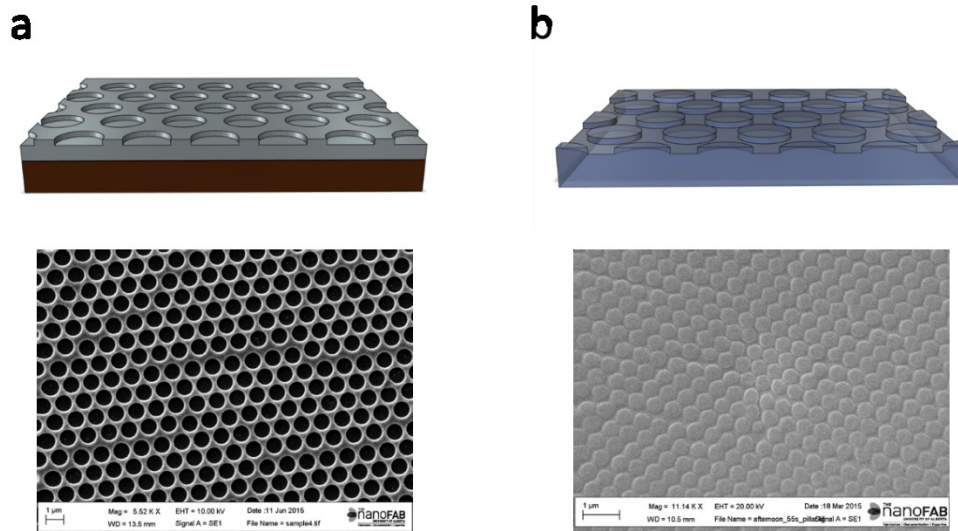
Figure 4.2 Top view SEM images and cross-sectional schematic of the nanocavity (a) and nanopillar (b) arrays fabricated.

4.2.2 The design of the PbS CQD solar cell with enhanced absorption

The periodic ITO electrodes proposed in this work are designed for a typical depleted heterojunction CQD solar cell structure. The depleted heterojunction architecture utilizes a TiO$_2$ layer as the n-side of the junction and p-type PbS quantum dots as the p-side. The bottom contact to the junction is formed on a glass substrate and consists of a thin transparent conductive ITO layer. The top contact employs a deep work function metal such as gold to collect photo-excited holes and also reflect back any unabsorbed photons into the light absorbing layer. A conformal layer of TiO$_2$ with thickness of 50 nm was considered as a layer between ITO electrode and active layer in simulation. The designed periodic nanostructures are implemented at the interface between the ITO bottom contact and PbS QDs. Figure 4.3 (a) shows the

schematic of the structure of PbS CQD solar cell with patterned ITO electrode used for simulation. As depicted in the figure, when the light is normally incident on ITO diffraction gratings through the transparent substrate, forward diffraction of light can induce light trapping by effectively increasing optical path lengths inside the absorbing material especially for higher diffracted orders supported by the grating structure. Optical constants of the materials used in the simulation model are shown in Figure 4.3 (b).
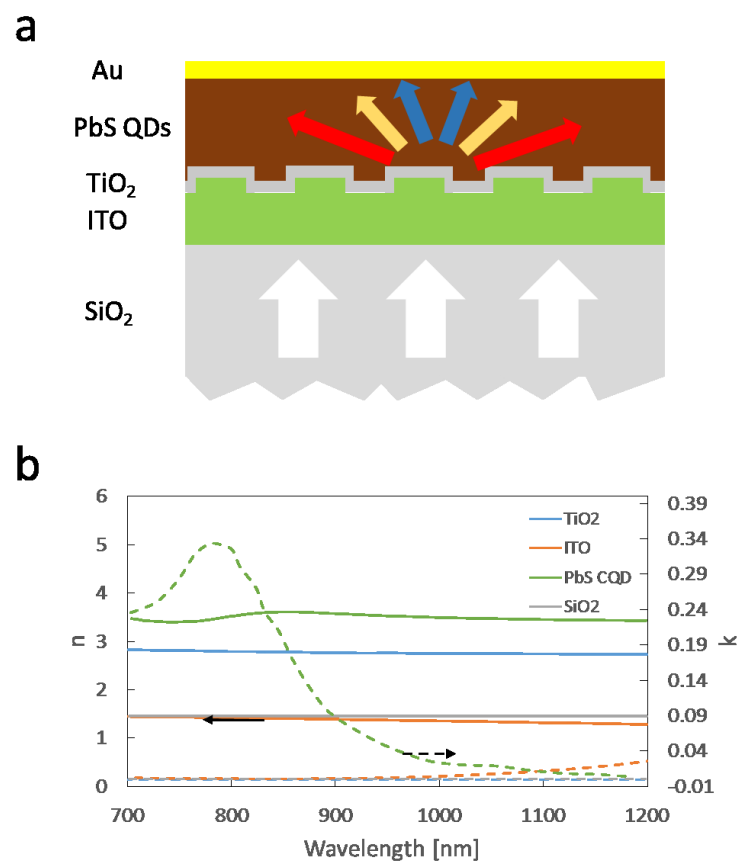
Figure 4.3 (a) Schematic of light diffraction in PbS QDs solar cell with patterned ITO electrode. (b) Optical constants of the materials used in the simulation model.

4.3   Light trapping analysis with FDTD simulation

The Lumerical FDTD Solutions software was used for simulations of the designed PbS CQD solar cell with identical structure shown in Figure 4.3 (a). A

period of 500 nm was chosen for both cavity and pillar structures which is same as the diameter of nanospheres used for pattern generation. A cavity depth and pillar height of 80 nm and a diameter of 360 nm for both structures was found to be an optimum value. The PbS CQD layer was considered to be a quasi-bulk homogeneous film (QDs were not considered as individual particles) without any voids and its thickness (excluding the nanostructure) was chosen to be 300 nm, which is usually considered as the optimum thickness for efficient photo-generated carrier collection. The TiO2 layer was assumed to be 50 nm thick. Both gold and SiO_2 glass layers were considered with infinite thickness for ease of modeling. The optimum thickness of ITO layer (excluding the nanostructure) was found to be 500 nm. It should be noted here that the periodic grating structure layer consists of both ITO and PbS materials. The multi-coefficient fitting tool inside the simulation software was utilized to model optical constants of materials from available experimental data.[17, 18] In the case of PbS QDs, the optical constants of commonly used QDs with a band-gap of 1.3 eV were used for simulations.

In addition to the solar cell structure applied in simulation, the light source was considered a plane wave source placed inside the substrate (SiO_2 layer) to simplify the simulations. The wavelength range of 700-1200 nm was chosen as the simulation wavelength span because PbS CQD solar cells are currently in need of absorption enhancement mostly in this region of sunlight.[18] For directions perpendicular to the incident light propagation direction, Bloch boundary conditions were used and for directions parallel to the light propagation direction, perfectly matched layer (PML) boundary conditions, which can be regarded as total absorption boundary, were defined. The amount of absorption inside the CQD layer was measured by placing two power monitors at the either sides of the layer. This configuration can calculate the power flow entering and exiting the layer and thus the power absorbed inside the layer can be obtained by calculating the difference between the

measurements from the two monitors.

Grating far-field projection analysis, which is an analysis tool to investigate the light diffraction through the periodic grating,[19] was firstly used to analyze the diffraction behavior of the proposed periodic grating structures in PbS CQD solar cells. The resulting transmission efficiencies of the simulated patterned structures are illustrated in Figure 4.4. For the transmission measurements, all the shown powers are normalized with respect to the power from the light source. As is clear from the figure, both cavity and pillar structures demonstrate high transmission efficiency in wavelength range of 700 nm to 900 nm. On the other hand, the amount of transmitted power is not significant beyond 900 nm. This trend, however, is broken for both nanocavity and nanopillar arrays at around the wavelength of 950 nm with a strong increase in the amount of transmitted power. The same behavior is also observed in the case of the cavity array at wavelength of 1080 nm, the intensity of which, however, is not as strong as the peak at 950 nm. This sudden increase in transmitted power can be attributed to the resonant coupling of the incident light into wave guiding modes supported by the PbS CQD layer through the patterned periodic cavity and pillar structures.[14] Although throughout the spectrum, a portion of incident light is not diffracted (shown as the order (0, 0)), by paying close attention to the total transmission values and their difference with order (0, 0), it is obvious that a significant amount of energy is diffracted into higher orders, especially at resonance wavelengths. This can greatly contribute to light absorption enhancement in CQD layer by increasing the optical path length of the light inside the layer or light trapping through resonant coupling with the incident light. The transmission efficiencies of two of the strongest diffracted orders (1, 1) and (2, 0) are also plotted in Figure 4.4.
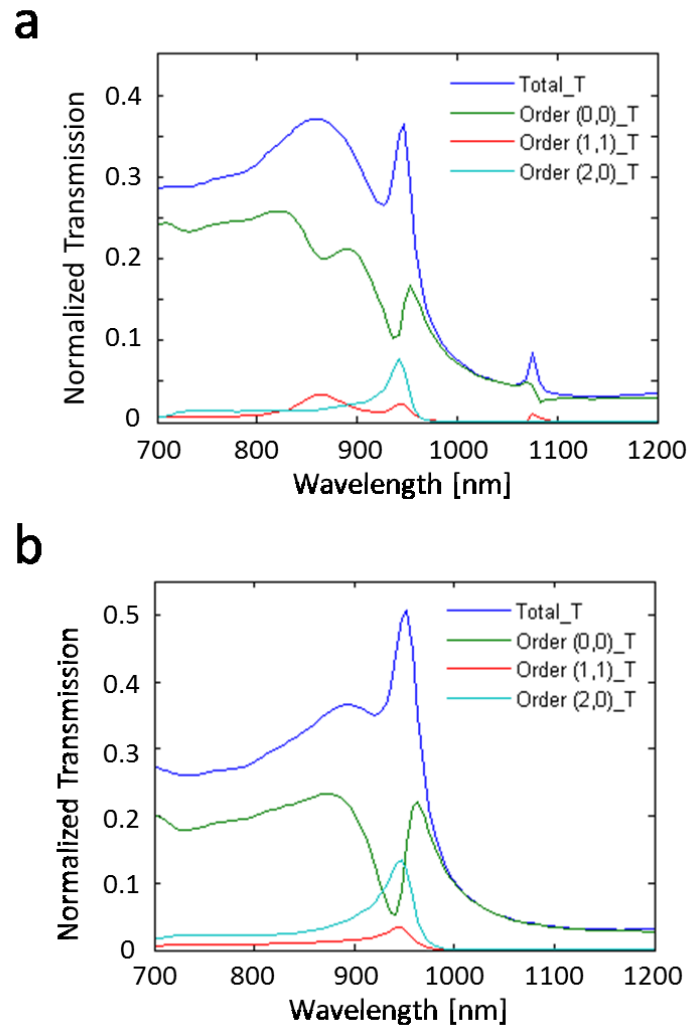
Figure 4.4 The normalized transmission spectra of simulated patterned ITO structures: (a) nanocavity (b) nanopillar. The plot shows the relative power transmitted into different diffracted orders and the total transmitted power normalized to the simulation source power. Two of the strongest diffracted orders (1,1) and (2,0) are plotted. (0,0) represents the part of incident power not being diffracted by the structures.

Figure 4.5 depicts the simulated light absorption spectra for PbS CQD layer of the modelled depleted heterojunction solar cell normalized to the AM1.5 solar spectrum (Figure 4.5 (a)) and simulation light source (Figure 4.5 (b)). In order to be able to compare the effect of proposed structures on absorption enhancement in PbS CQD layer, a flat ITO layer was considered as the reference. The available power from AM1.5G[20] spectrum is also included in the figure for comparison. As is

63

obvious from the figure, both nanocavity and nanopillar arrays can induce more light absorption in CQD layer than the flat ITO layer within most parts of the near-infrared region. It is also noticeable that both proposed structures have achieved almost perfect absorption in the range of 720 nm to 850 nm by absorbing all the power available from the sun in this range. As for beyond this range, especially in the case of cavity structure, the resonant coupling of the incident light into guided modes supported by CQD layer is the major responsible for strong but narrowband absorption enhancements at resonant peaks, previously predicted by grating projection analysis. This is possible because of the major difference in refractive indices of the CQD layer and the ITO layer which can form an efficient waveguide in the middle of the cell's structure.

In order to have an overall evaluation for the light absorption enhancement performance of the proposed structures, the average absorption enhancement of the structures over the entire simulated spectrum was measured against the flat reference structure using the following equation:

$$Absorption\ enhancement = \frac{P_g - P_r}{P_r} \times 100\% \qquad (4.1)$$

where P_g depicts the total power absorbed by the cell with grating structure and P_r denotes the power absorbed in flat structure. According to the equation, the calculated absorption enhancement factors for nanocavity and nanopillar grating structures compared to the flat structure are 15.0% and 13.6%, respectively. This amount of absorption enhancement can significantly boost charge carrier generation and thus short-circuit current density of a CQD solar cell which can ultimately lead to remarkable improvement in power conversion efficiency of the solar cell.
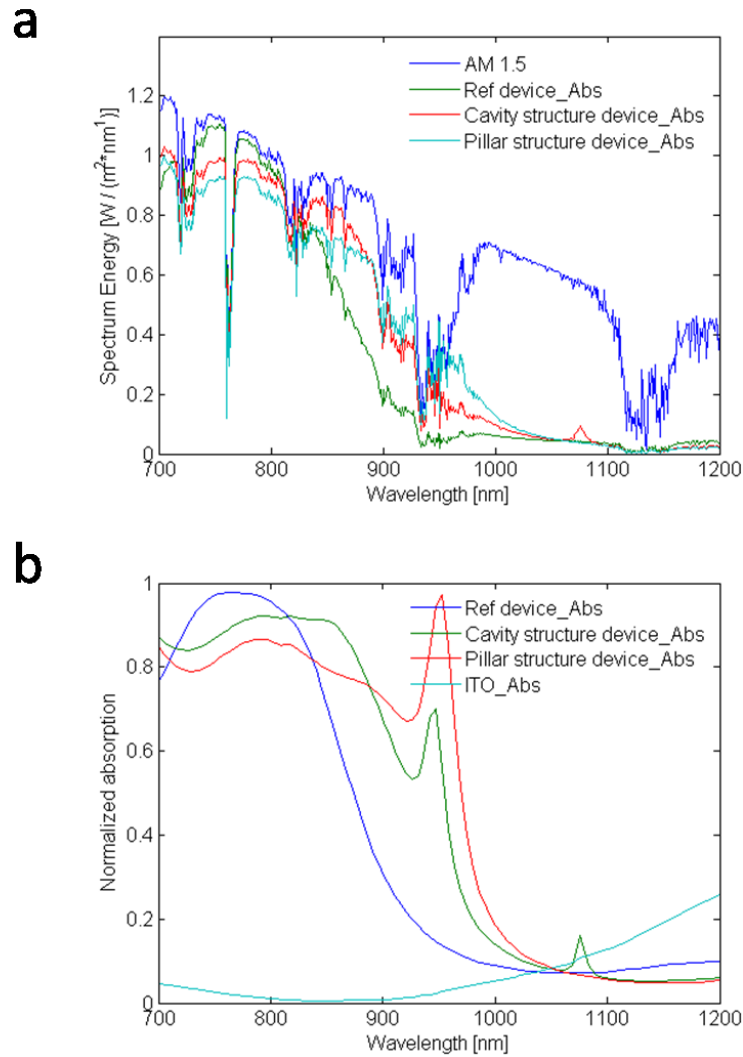
Figure 4.5 The light absorption spectra for PbS CQD layer incorporated into different ITO structures normalized to (a) AM1.5 spectra and (b) simulation light source. The absorption enhancement for both cavity and pillar structures over the reference flat structure is obvious especially at resonance wavelengths of 950 nm for both structures. A slight absorption loss by ITO electrode was also observed.

To clearly demonstrate the influence of nanocavity and nanopillar resonance effect on absorption enhancement in CQD layer, the electric field distributions inside the PbS CQD layer with patterned structures were investigated and are shown in Figure 4.6. The on resonance profiles for nanocavity and nanopillar structures are plotted at wavelength of 950 nm and the off resonant profile wavelength is chosen at

1000 nm for both structures. The on resonance profiles for both structures reveal various absorption hot spots for on-resonance wavelengths where as in the case of off resonance profiles, no hot spot is visible at off-resonance wavelengths. It is obvious that the presence of high intensity E-field spots (hot spots) indicates the occurrence of strong absorption inside PbS CQD layer. In addition, the periodic pattern of the hot spots observed in the obtained profiles discloses the type of resonance to be the guided mode kind usually excited by periodic dielectric nanostructures.[6] The difference in field distribution observed between on and off resonance profiles implies the impressive light trapping performance of the proposed structures at resonance wavelengths. This confirms the superiority of the proposed structures for absorption enhancement in CQD solar cells through resonant coupling of the incident light with supported waveguide modes inside the CQD layer.
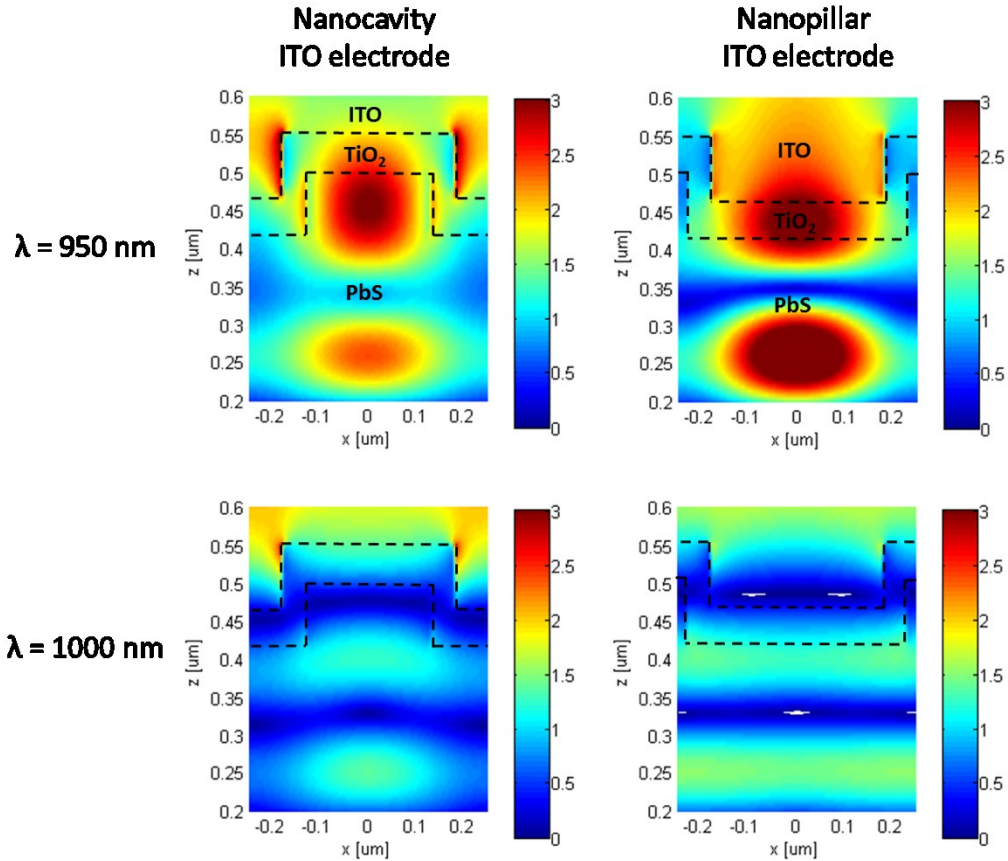
Figure 4.6 Simulated electric field distributions inside the PbS QDs layer with patterned structures. The hot spots present at resonance wavelengths (950 nm for both structures) with high field intensity indicate strong absorption inside PbS CQD. No hot spots are observed at off resonance wavelengths (1000 nm for both structures) suggesting the importance of resonant coupling of the incident into CQD layer for significant absorption enhancement.

4.4   Summary

In conclusion, ITO nanocavity and nanopillar arrays are proposed as light trapping structures in CQD solar cells to realize absorption enhancement and power conversion efficiency improvement. A simple fabrication process of large area nanocavity and nanopillar array is demonstrated. The simulation results show that both proposed periodic structures can effectively increase the light absorption in CQD layer of the solar cell throughout the near-infrared region where CQD solar

cells typically exhibit weak light absorption. The overall absorption enhancement of 15.0% and 13.6% was achieved for nanocavity and nanopillar structures, respectively. The simulated absorption enhancement in PbS CQD solar cell proves the feasibility of the application of large area LTS in CQD thin film solar cells.

Reference

1.   Chang, L.-Y., et al., *Low-Temperature Solution-Processed Solar Cells Based on PbS Colloidal Quantum Dot/CdS Heterojunctions.* Nano Letters, 2013. **13**(3): p. 994-999.

2.   Tang, J. and E.H. Sargent, *Infrared Colloidal Quantum Dots for Photovoltaics: Fundamentals and Recent Progress.* Advanced Materials, 2011. **23**(1): p. 12-29.

3.   Clifford, J.P., et al., *Fast, sensitive and spectrally tuneable colloidal-quantum-dot photodetectors.* Nat Nano, 2009. **4**(1): p. 40-44.

4.   Zhitomirsky, D., et al., *Measuring Charge Carrier Diffusion in Coupled Colloidal Quantum Dot Solids.* ACS Nano, 2013. **7**(6): p. 5282-5290.

5.   Labelle, A.J., et al., *Conformal Fabrication of Colloidal Quantum Dot Solids for Optically Enhanced Photovoltaics.* ACS Nano, 2015. **9**(5): p. 5447-5453.

6.   Brongersma, M.L., Y. Cui, and S. Fan, *Light management for photovoltaics using high-index nanostructures.* Nat Mater, 2014. **13**(5): p. 451-460.

7.   Cao, S., et al., *Two-dimensional subwavelength meta-nanopillar array for efficient visible light absorption.* Applied Physics Letters, 2013. **102**(16): p. 161109.

8.   Han, Q., et al., *Si substrate-based metamaterials for ultrabroadband perfect absorption in visible regime.* J. Nanomaterials, 2015. **2014**: p. 232-232.

9.   Han, S.E. and G. Chen, *Optical Absorption Enhancement in Silicon Nanohole Arrays for Solar Photovoltaics.* Nano Letters, 2010. **10**(3): p. 1012-1015.

10.   Atwater, H.A. and A. Polman, *Plasmonics for improved photovoltaic devices.* Nat Mater, 2010. **9**(3): p. 205-213.

11.   Ding, I.K., et al., *Plasmonic Dye-Sensitized Solar Cells.* Advanced Energy Materials, 2011. **1**(1): p. 52-57.

12.   Min, C., et al., *Enhancement of optical absorption in thin-film organic solar cells through the excitation of plasmonic modes in metallic gratings.* Applied Physics Letters, 2010. **96**(13): p. 133302.

13.   Raman, A., Z. Yu, and S. Fan, *Dielectric nanostructures for broadband light trapping in organic solar cells.* Optics Express, 2011. **19**(20): p. 19015-19026.

14.   Mahpeykar, S.M., Q. Xiong, and X. Wang, *Resonance-induced absorption enhancement in colloidal quantum dot solar cells using nanostructured electrodes.* Optics Express, 2014. **22**(S6): p. A1576-A1588.

15.   Hall, A.S., S.A. Friesen, and T.E. Mallouk, *Wafer-Scale Fabrication of Plasmonic Crystals from Patterned Silicon Templates Prepared by Nanosphere Lithography.* Nano Letters, 2013. **13**(6): p. 2623-2627.

16.   Yang, S., et al., *Large-Scale Fabrication of Three-Dimensional Surface Patterns Using Template-Defined Electrochemical Deposition.* Advanced Functional Materials, 2013. **23**(6): p. 720-730.

17.   Synowicki, R.A., *Spectroscopic ellipsometry characterization of indium tin oxide film microstructure and optical constants.* Thin Solid Films, 1998. **313–314**: p. 394-397.

18.   Wang, X., et al., *Tandem colloidal quantum dot solar cells employing a graded recombination layer.* Nat Photon, 2011. **5**(8): p. 480-484.

19.   Lumerical Solution Inc. *Grating projection*. 2016; Available from: http://docs.lumerical.com/en/solvers_grating_projections.html.

20.   Reference Solar Spectral Irradiance. *ASTM G-173*. 2016; Available from: http://rredc.nrel.gov/solar/spectra/am1.5/ASTMG173/ASTMG173.html.

Chapter 5. Conclusion and future works

5.1 Summary and results

This chapter concludes the experimental and simulation works about the 2D grating and its application in PbS CQD cells. The fabrication process for large area 2D pattern has been optimized step by step and high quality nanocavity and nanopillar grating structures have been achieved. With the fabricated Ag grating, the properties of the excited SP have been investigated with both experiment and simulation approaches to figure out the feasibility of such structure as the back reflector of thin film solar cells. Finally, the study of integrating 2D structures with PbS CQD solar cells has been accomplished using FDTD simulation. The presence of nanostructures has greatly improved the light absorption of the PbS CQD device.

5.1.1 Fabrication of 2D nanostructure with NSL

Large area 2D mask was successfully fabricated with the self-assembled nanospheres at water-air interface. For the 500 nm nanospheres, the best suspension composition is 1:1 mixture of 3% w/w sphere water suspension and the ethanol. During the mask formation, the dispersion stage is required to be placed close to the edge of the petri dish to control nanosphere flowing direction for better mask quality. Additionally, the oxygen RIE treatment is proven to be a feasible approach to shrink the nanospheres and lower oxygen flow rate is preferable for precise control of nanosphere size. Most of all, all factors including mask quality, substrate hydrophilicity and targeting nanostructure configuration should be comprehensively investigated to get a well patterned structure.

5.1.2 Surface plasmon excitation on 2D Ag gratings

The property of the SP on the 2D Ag grating was investigated in details with experiment and simulation. The key conclusions are summarized below:

1. The LSP and SPP were observed to be excited on the Ag grating surface. Strong SPP and LSP hybridization was observed as the resonant frequency of the two SP modes get closer. The existence of LSP on the Ag grating was further justified with a controlled experiment using the SiO_2 grating.

2. Two SPP modes were observed on the Ag grating, corresponding to the different SPP modes with different propagating directions.

3. Great E-field intensity near the Ag grating upon SP resonant frequency was confirmed with the FDTD simulation, showing the potential for the application of such structure as the solar cell back reflector.

5.1.3 PbS CQD solar cells with patterned ITO electrodes

The nanocavity and nanopillar arrays were proposed for ITO electrodes in PbS CQD solar cells. Detailed fabrication process was provided and the absorption enhancement in the PbS CQD absorbing layer was simulated with FDTD simulation. The obtained key results are provided below:

1. The integration of patterned ITO electrodes was proven to be a good way to increase the PCE of PbS CQD cells for more light absorbed in the active layer. The absorption was enhanced by the incident light energy redistribution into different diffraction orders and effective transmission path was increased.

2. According to simulation, the nanocavity and nanopillar array resulted in an overall absorption enhancement of 15% and 13.6% in the PbS CQD layer, respectively. The absorption of PbS CQD in near-infrared region was greatly

increased.

5.2 Future works

The fabrication of large area 2D nanostructures was successfully demonstrated in the previous work. Meanwhile, the preliminary application of LST in PbS CQD cells has been investigated. According to our study, the nanostructures show great potential in improving the performance of thin film PbS CQD solar cells, but there are still lots of works to be done in the future. Some follow-up works on LST assisted PbS CQD solar cells are proposed below:

1. The fabrication of nanosphere mask can be further optimized to achieve better light scattering effect. The defects observed in the fabricated structures, which is caused by the deformation of mask during water evaporation can be reduced by adding an additional mask annealing step. In addition, the fabrication of mask using nanospheres of different sizes is also necessary for diverse applications in the future.

2. The fabricated 2D Ag grating can be integrated with real PbS CQD solar cells as the back reflector. The simulation results have given a guidance on how the metallic grating interacts with light and what should be taken care of during the device fabrication. Although the PbS CQD layer can be easily formed on the structure layer with ligand exchange process, the integration of nanostrcuture into the PV device still faces a lot of challenges.

3. The patterned ITO electrode can be fabricated and applied into PbS CQD solar cells using the device architecture proposed in the thesis.

Nowadays, the periodic nanostructures have more applications in various fields other than solar cells. In the future, the 2D nanostructures and fabrication methods developed in the thesis may extend their applications to other research fields.

Reference

1.   McDonald, S.A., et al., *Solution-processed PbS quantum dot infrared photodetectors and photovoltaics.* Nat Mater, 2005. **4**(2): p. 138-142.

2.   Ferry, V.E., et al., *Light trapping in ultrathin plasmonic solar cells.* Optics Express, 2010. **18**(S2): p. A237-A245.

3.   Müller, J., et al., *TCO and light trapping in silicon thin film solar cells.* Solar Energy, 2004. **77**(6): p. 917-930.

4.   Law, M., et al., *Nanowire dye-sensitized solar cells.* Nat Mater, 2005. **4**(6): p. 455-459.

5.   Anna Selvan, J.A., et al., *A new light trapping TCO for nc-Si:H solar cells.* Solar Energy Materials and Solar Cells, 2006. **90**(18–19): p. 3371-3376.

6.   Zhou, D. and R. Biswas, *Photonic crystal enhanced light-trapping in thin film solar cells.* Journal of Applied Physics, 2008. **103**(9): p. 093102.

7.   Atwater, H.A. and A. Polman, *Plasmonics for improved photovoltaic devices.* Nat Mater, 2010. **9**(3): p. 205-213.

8.   Garnett, E. and P. Yang, *Light Trapping in Silicon Nanowire Solar Cells.* Nano Letters, 2010. **10**(3): p. 1082-1087.

9.   Yafei, Z., et al., *Development of Inorganic Solar Cells by Nanotechnology.* Nano-Micro Letters, 2012. **4**(2): p. 124-134.

10.   OECD, *Electricity generation.* OECD Publishing.

11.   Hoffert, M.I., et al., *Energy implications of future stabilization of atmospheric CO2 content.* Nature, 1998. **395**(6705): p. 881-884.

12.   Callahan, D.M., J.N. Munday, and H.A. Atwater, *Solar Cell Light Trapping beyond the Ray Optic Limit.* Nano Letters, 2012. **12**(1): p. 214-218.

13.   Campbell, P. and M.A. Green, *Light trapping properties of pyramidally textured surfaces.* Journal of Applied Physics, 1987. **62**(1): p. 243-249.

14.   Teck Kong, C., et al., *Optimal wavelength scale diffraction gratings for light trapping in solar cells.* Journal of Optics, 2012. **14**(2): p. 024012.

15.   Aberle, A.G., *Thin-film solar cells.* Thin Solid Films, 2009. **517**(17): p. 4706-4710.

16.   Goetzberger, A., *Optical confinement in thin Si solar cells by diffuse back reflectors*, in *15th Photovoltaic Specialists Conference*. 1981: Kissimmee, FL. p. 867-870.

17.   Yablonovitch, E., *Statistical ray optics.* Journal of the Optical Society of America, 1982. **72**(7): p. 899-907.

18.   Battaglia, C., et al., *Light Trapping in Solar Cells: Can Periodic Beat Random?* ACS Nano, 2012. **6**(3): p. 2790-2797.

19.   Yu, Z., A. Raman, and S. Fan, *Fundamental limit of nanophotonic light trapping in solar cells.* Proceedings of the National Academy of Sciences, 2010. **107**(41): p. 17491-17496.

20.   National Center for Photovoltaics. *Research Cell Efficiency Records*. 2016; Available from: http://www.nrel.gov/ncpv/.

21.   Jean, J., et al., *ZnO Nanowire Arrays for Enhanced Photocurrent in PbS Quantum Dot Solar Cells.* Advanced Materials, 2013. **25**(20): p. 2790-2796.

22.   Barkhouse, D.A.R., et al., *Depleted Bulk Heterojunction Colloidal Quantum Dot Photovoltaics.* Advanced Materials, 2011. **23**(28): p. 3134-3138.

23.   Kramer, I.J., et al., *Ordered Nanopillar Structured Electrodes for Depleted Bulk Heterojunction Colloidal Quantum Dot Solar Cells.* Advanced Materials, 2012. **24**(17): p. 2315-2319.

24.   Adachi, M.M., et al., *Broadband solar absorption enhancement via periodic nanostructuring of electrodes.* Scientific Reports, 2013. **3**: p. 2928.

25.   Mahpeykar, S.M., Q. Xiong, and X. Wang, *Resonance-induced absorption enhancement in colloidal quantum dot solar cells using nanostructured electrodes.* Optics Express, 2014. **22**(S6): p. A1576-A1588.

26.   Paz-Soldan, D., et al., *Jointly Tuned Plasmonic–Excitonic Photovoltaics Using Nanoshells.* Nano Letters, 2013. **13**(4): p. 1502-1508.

27.   Vieu, C., et al., *Electron beam lithography: resolution limits and applications.* Applied Surface Science, 2000. **164**(1–4): p. 111-117.

28.   Hulteen, J.C. and R.P. Van Duyne, *Nanosphere lithography: A materials general fabrication process for periodic particle array surfaces.* Journal of Vacuum Science & Technology A, 1995. **13**(3): p. 1553-1558.

29.   Fischer, U.C. and H.P. Zingsheim, *Submicroscopic pattern replication with visible light.* Journal of Vacuum Science & Technology, 1981. **19**(4): p. 881-885.

30.   Battaglia, C., et al., *Nanomoulding of transparent zinc oxide electrodes for efficient light trapping in solar cells.* Nat Photon, 2011. **5**(9): p. 535-538.

31.   Ji, R., et al., *UV enhanced substrate conformal imprint lithography (UV-SCIL) technique for photonic crystals patterning in LED manufacturing.* Microelectronic Engineering, 2010. **87**(5–8): p. 963-967.

32.   Hornung, M., et al. *6 inch full field wafer size nanoimprint lithography for photonic crystals patterning.* in *Nanotechnology (IEEE-NANO), 2010 10th IEEE Conference on.* 2010.

33.   Kang, M.-G., et al., *Organic Solar Cells Using Nanoimprinted Transparent Metal Electrodes.* Advanced Materials, 2008. **20**(23): p. 4408-4413.

34.   Dill, F.H., *Optical lithography.* IEEE Transactions on Electron Devices, 1975. **22**(7): p. 440-444.

35.   Rothschild, M., et al., *Lithography at a wavelength of 193 nm.* IBM Journal of Research and Development, 1997. **41**(1.2): p. 49-55.

36.   Chou, S.Y., P.R. Krauss, and P.J. Renstrom, *Nanoimprint lithography.* Journal of Vacuum Science & Technology B, 1996. **14**(6): p. 4129-4133.

37.   Pease, R.F.W., *Electron beam lithography.* Contemporary Physics, 1981. **22**(3): p. 265-290.

38.   Melngailis, J., *Focused ion beam lithography*. Nuclear Instruments and Methods in Physics Research Section B: Beam Interactions with Materials and Atoms, 1993. **80**: p. 1271-1280.

39.   Gates, B.D., et al., *New Approaches to Nanofabrication: Molding, Printing, and Other Techniques*. Chemical Reviews, 2005. **105**(4): p. 1171-1196.

40.   Hennessy, K., et al., *Square-lattice photonic crystal microcavities for coupling to single InAs quantum dots*. Applied Physics Letters, 2003. **83**(18): p. 3650-3652.

41.   Zhu, X., et al., *Ultrafine and Smooth Full Metal Nanostructures for Plasmonics*. Advanced Materials, 2010. **22**(39): p. 4345-4349.

42.   Kosiorek, A., et al., *Shadow Nanosphere Lithography: Simulation and Experiment*. Nano Letters, 2004. **4**(7): p. 1359-1363.

43.   Li, H., et al., *Large-Area Well-Ordered Nanodot Array Pattern Fabricated With Self-Assembled Nanosphere Template*. IEEE Sensors Journal, 2008. **8**(6): p. 880-884.

44.   Haynes, C.L., et al., *Angle-Resolved Nanosphere Lithography: Manipulation of Nanoparticle Size, Shape, and Interparticle Spacing*. The Journal of Physical Chemistry B, 2002. **106**(8): p. 1898-1902.

45.   Schäfer, C.G., et al., *Fully Reversible Shape Transition of Soft Spheres in Elastomeric Polymer Opal Films*. Langmuir, 2013. **29**(36): p. 11275-11283.

46.   Shiu, J.-Y., et al., *Fabrication of Tunable Superhydrophobic Surfaces by Nanosphere Lithography*. Chemistry of Materials, 2004. **16**(4): p. 561-564.

47.   Kosiorek, A., et al., *Fabrication of Nanoscale Rings, Dots, and Rods by Combining Shadow Nanosphere Lithography and Annealed Polystyrene Nanosphere Masks*. Small, 2005. **1**(4): p. 439-444.

48.   Haes, A.J., et al., *Solution-Phase, Triangular Ag Nanotriangles Fabricated by Nanosphere Lithography*. The Journal of Physical Chemistry B, 2005. **109**(22): p. 11158-11162.

49.   Hulteen, J.C., et al., *Nanosphere Lithography: Size-Tunable Silver Nanoparticle and Surface Cluster Arrays.* The Journal of Physical Chemistry B, 1999. **103**(19): p. 3854-3863.

50.   Hering, K., et al., *SERS: a versatile tool in chemical and biochemical diagnostics.* Analytical and Bioanalytical Chemistry, 2008. **390**(1): p. 113-124.

51.   Schmidt, J.P., S.E. Cross, and S.K. Buratto, *Surface-enhanced Raman scattering from ordered Ag nanocluster arrays.* The Journal of Chemical Physics, 2004. **121**(21): p. 10657-10659.

52.   Debnath, R., et al., *Ambient-Processed Colloidal Quantum Dot Solar Cells via Individual Pre-Encapsulation of Nanoparticles.* Journal of the American Chemical Society, 2010. **132**(17): p. 5952-5953.

53.   Jensen, T.R., et al., *Nanosphere Lithography: Effect of the External Dielectric Medium on the Surface Plasmon Resonance Spectrum of a Periodic Array of Silver Nanoparticles.* The Journal of Physical Chemistry B, 1999. **103**(45): p. 9846-9853.

54.   Cheung, C.L., et al., *Fabrication of nanopillars by nanosphere lithography.* Nanotechnology, 2006. **17**(5): p. 1339.

55.   Yu, J., et al., *Preparation of High-Quality Colloidal Mask for Nanosphere Lithography by a Combination of Air/Water Interface Self-Assembly and Solvent Vapor Annealing.* Langmuir, 2012. **28**(34): p. 12681-12689.

56.   Chen, W., R.H.W. Lam, and J. Fu, *Photolithographic surface micromachining of polydimethylsiloxane (PDMS).* Lab on a chip, 2012. **12**(2): p. 391-395.

57.   Hall, A.S., S.A. Friesen, and T.E. Mallouk, *Wafer-Scale Fabrication of Plasmonic Crystals from Patterned Silicon Templates Prepared by Nanosphere Lithography.* Nano Letters, 2013. **13**(6): p. 2623-2627.

58.   Ritchie, R.H., *Plasma Losses by Fast Electrons in Thin Films.* Physical Review, 1957. **106**(5): p. 874-881.

59.   Ebbesen, T.W., et al., *Extraordinary optical transmission through sub-wavelength hole arrays.* Nature, 1998. **391**(6668): p. 667-669.

60.   Tanaka, K. and M. Tanaka, *Simulations of nanometric optical circuits based on surface plasmon polariton gap waveguide.* Applied Physics Letters, 2003. **82**(8): p. 1158-1160.

61.   Anker, J.N., et al., *Biosensing with plasmonic nanosensors.* Nat Mater, 2008. **7**(6): p. 442-453.

62.   Yang, J., et al., *Plasmonic Polymer Tandem Solar Cell.* ACS Nano, 2011. **5**(8): p. 6210-6217.

63.   Aydin, K., et al., *Broadband polarization-independent resonant light absorption using ultrathin plasmonic super absorbers.* Nat Commun, 2011. **2**: p. 517.

64.   Chu, Y., M.G. Banaee, and K.B. Crozier, *Double-Resonance Plasmon Substrates for Surface-Enhanced Raman Scattering with Enhancement at Excitation and Stokes Frequencies.* ACS Nano, 2010. **4**(5): p. 2804-2810.

65.   Myroshnychenko, V., et al., *Modelling the optical response of gold nanoparticles.* Chemical Society Reviews, 2008. **37**(9): p. 1792-1805.

66.   Maier, S.A., *Plasmonics: Fundamentals and Applications*. 2010: Springer US.

67.   Félidj, N., et al., *Multipolar surface plasmon peaks on gold nanotriangles.* The Journal of Chemical Physics, 2008. **128**(9): p. 094702.

68.   Höflich, K., U. Gösele, and S. Christiansen, *Near-field investigations of nanoshell cylinder dimers.* The Journal of Chemical Physics, 2009. **131**(16): p. 164704.

69.   Nishijima, Y., et al., *Plasmon-Assisted Photocurrent Generation from Visible to Near-Infrared Wavelength Using a Au-Nanorods/TiO2 Electrode.* The Journal of Physical Chemistry Letters, 2010. **1**(13): p. 2031-2036.

70.   Ferry, V.E., et al., *Optimized Spatial Correlations for Broadband Light Trapping Nanopatterns in High Efficiency Ultrathin Film a-Si:H Solar Cells.* Nano Letters, 2011. **11**(10): p. 4239-4245.

71.   Chu, Y. and K.B. Crozier, *Experimental study of the interaction between localized and propagating surface plasmons.* Optics Letters, 2009. **34**(3): p. 244-246.

72.   Sarkar, M., et al., *Hybrid Plasmonic Mode by Resonant Coupling of Localized Plasmons to Propagating Plasmons in a Kretschmann Configuration.* ACS Photonics, 2015. **2**(2): p. 237-245.

73.   Peng, K., et al., *Ordered silicon nanowire arrays via nanosphere lithography and metal-induced etching.* Applied Physics Letters, 2007. **90**(16): p. 163123.

74.   Iwata, K., et al., *Three-dimensional profiling using the Fourier transform method with a hexagonal grating projection.* Applied Optics, 2008. **47**(12): p. 2103-2108.

75.   Johnson, P.B. and R.W. Christy, *Optical Constants of the Noble Metals.* Physical Review B, 1972. **6**(12): p. 4370-4379.

76.   Chang, L.-Y., et al., *Low-Temperature Solution-Processed Solar Cells Based on PbS Colloidal Quantum Dot/CdS Heterojunctions.* Nano Letters, 2013. **13**(3): p. 994-999.

77.   Tang, J. and E.H. Sargent, *Infrared Colloidal Quantum Dots for Photovoltaics: Fundamentals and Recent Progress.* Advanced Materials, 2011. **23**(1): p. 12-29.

78.   Clifford, J.P., et al., *Fast, sensitive and spectrally tuneable colloidal-quantum-dot photodetectors.* Nat Nano, 2009. **4**(1): p. 40-44.

79.   Zhitomirsky, D., et al., *Measuring Charge Carrier Diffusion in Coupled Colloidal Quantum Dot Solids.* ACS Nano, 2013. **7**(6): p. 5282-5290.

80.   Labelle, A.J., et al., *Conformal Fabrication of Colloidal Quantum Dot Solids for Optically Enhanced Photovoltaics.* ACS Nano, 2015. **9**(5): p. 5447-5453.

81.   Brongersma, M.L., Y. Cui, and S. Fan, *Light management for photovoltaics using high-index nanostructures.* Nat Mater, 2014. **13**(5): p. 451-460.

82.   Cao, S., et al., *Two-dimensional subwavelength meta-nanopillar array for efficient visible light absorption.* Applied Physics Letters, 2013. **102**(16): p. 161109.

83.   Han, Q., et al., *Si substrate-based metamaterials for ultrabroadband perfect absorption in visible regime.* J. Nanomaterials, 2015. **2014**: p. 232-232.

84.   Han, S.E. and G. Chen, *Optical Absorption Enhancement in Silicon Nanohole Arrays for Solar Photovoltaics.* Nano Letters, 2010. **10**(3): p. 1012-1015.

85.   Ding, I.K., et al., *Plasmonic Dye-Sensitized Solar Cells.* Advanced Energy Materials, 2011. **1**(1): p. 52-57.

86.   Min, C., et al., *Enhancement of optical absorption in thin-film organic solar cells through the excitation of plasmonic modes in metallic gratings.* Applied Physics Letters, 2010. **96**(13): p. 133302.

87.   Raman, A., Z. Yu, and S. Fan, *Dielectric nanostructures for broadband light trapping in organic solar cells.* Optics Express, 2011. **19**(20): p. 19015-19026.

88.   Yang, S., et al., *Large-Scale Fabrication of Three-Dimensional Surface Patterns Using Template-Defined Electrochemical Deposition.* Advanced Functional Materials, 2013. **23**(6): p. 720-730.

89.   Synowicki, R.A., *Spectroscopic ellipsometry characterization of indium tin oxide film microstructure and optical constants.* Thin Solid Films, 1998. **313–314**: p. 394-397.

90.   Wang, X., et al., *Tandem colloidal quantum dot solar cells employing a graded recombination layer.* Nat Photon, 2011. **5**(8): p. 480-484.

91.   Lumerical Solution Inc. *Grating projection.* 2016; Available from: http://docs.lumerical.com/en/solvers_grating_projections.html.

92.   Reference Solar Spectral Irradiance. *ASTM G-173.* 2016; Available from: http://rredc.nrel.gov/solar/spectra/am1.5/ASTMG173/ASTMG173.html.